Health Monitoring
for Graphite/Epoxy Motor Cases

15 May 2000

Edited by

R. P. WELLE
Laboratory Operations

Prepared for

SPACE AND MISSILE SYSTEMS CENTER
AIR FORCE MATERIEL COMMAND
2430 E. El Segundo Boulevard
Los Angeles Air Force Base, CA 90245

20000905 051

Engineering and Technology Group

**THE AEROSPACE
CORPORATION**
El Segundo, California

DTIC QUALITY INSPECTED

1 Lt Brent Shepherd, USAF
SMC/CLM

REPORT DOCUMENTATION PAGE

Public reporting burden for this collection of information is estimated to average 1 hour per response, including the time for reviewing instructions, searching existing data sources, gathering and maintaining the data needed, and completing and reviewing the collection of information. Send comments regarding this burden estimate or any other aspect of this collection of information, including suggestions for reducing this burden to Washington Headquarters Services, Directorate for Information Operations and Reports, 1215 Jefferson Davis Highway, Suite 1204, Arlington, VA 22202-4302, and to the Office of Management and Budget, Paperwork Reduction Project (0704-0188), Washington, DC 20503.

1. AGENCY USE ONLY (*Leave blank*)	2. REPORT DATE 15 May 2000	3. REPORT TYPE AND DATES COVERED

4. TITLE AND SUBTITLE

Health Monitoring for Graphite/Epoxy Motor Cases

5. FUNDING NUMBERS

F04701-93-C-0094

6. AUTHOR(S)

R. P. Welle, Editor

7. PERFORMING ORGANIZATION NAME(S) AND ADDRESS(ES)

The Aerospace Corporation
Laboratory Operations
El Segundo, CA 90245-4691

8. PERFORMING ORGANIZATION REPORT NUMBER

TR-2000(1222)-1

9. SPONSORING/MONITORING AGENCY NAME(S) AND ADDRESS(ES)

Space and Missile Systems Center
Air Force Materiel Command
2430 E. El Segundo Boulevard
Los Angeles Air Force Base, CA 90245

10. SPONSORING/MONITORING AGENCY REPORT NUMBER

SMC-TR-00-26

11. SUPPLEMENTARY NOTES

12a. DISTRIBUTION/AVAILABILITY STATEMENT

Approved for public release; distribution unlimited

12b. DISTRIBUTION CODE

13. ABSTRACT (*Maximum 200 words*)

This document is a compilation of the final reports prepared by the principal investigators in a series of experiments aimed at investigating the utility of a health monitoring system for solid rocket motor cases. Some of these reports have been published independently. The goal of this document is to bring all these reports together in an archival format and to provide a summary of their results.

14. SUBJECT TERMS

Delta, GEM, Graphite/Epoxy, Health Monitoring, MEMS, Fiber Optics, Acoustic Emission.

15. NUMBER OF PAGES

57

16. PRICE CODE

17. SECURITY CLASSIFICATION OF REPORT UNCLASSIFIED	18. SECURITY CLASSIFICATION OF THIS PAGE UNCLASSIFIED	19. SECURITY CLASSIFICATION OF ABSTRACT UNCLASSIFIED	20. LIMITATION OF ABSTRACT

NSN 7540-01-280-5500

Preface

This document is a compilation of the final reports prepared by the principal investigators in a series of experiments aimed at investigating the utility of a health monitoring system for solid rocket motor cases. Some of these reports have been published independently. The goal of this document is to bring all these reports together in an archival format and to provide a summary of their results.

Concurrence Signature Sheet

2.	Impact Monitoring and Reference Strain
	Measurement Using Conventional Resistance
	Strain Gages (L. H. Wiedeman)

3.	Impact Sensing with Fiber-Optic Bragg Grating
	Sensors (C. M. Klimcak, Y. Chan)

4.	Measurements of Acceleration on Delta GEM
	Boosters (S. T. Amimoto, D. J. Chang, E. W.
	Fournier, E. M. Yohnsee)

5.	Acoustic Emission Testing of the Delta
	Graphite/Epoxy Rocket Motor (GEM) (J. P.
	Nokes)

6.	Full-Scale DELTA GEM MPS Demonstration
	(J. V. Osborn, B. C. Brown, S. T. Amimoto, E.
	W. Fournier)

Contents

Figures

Tables

1. Introduction and Executive Summary (R. P. Welle)

Composite solid rocket motor cases made with graphite/epoxy matrix offer significant performance advantages over traditional steel cases, but are susceptible to catastrophic failure due to impact damage. Such damage can occur anywhere in the preparation and handling of the motors, and is not necessarily apparent, even to a trained observer, prior to launch. On 17 January 1997, a Delta II launch vehicle (flight 241) was destroyed about 13 seconds after launch due to a pressure rupture of the case of one of the Graphite/Epoxy Motor (GEM) strap-on boosters. A failure review board concluded that the case had been damaged by an unknown impact event prior to launch. As such, the development of means for preventing such failures in the future has become a high priority.

There are three basic routes available for preventing such incidents. First, the fabrication and handling processes are designed to minimize any possibility of impact events. Second, the cases are given a detailed inspection as late as possible prior to launch. Third, a monitoring system is established that will detect any unusual events and notify the appropriate authorities. To some extent, all these routes have been implemented for the Delta GEM. The fabrication and handling process for the Delta GEM have already been thought out in detail, and are carefully specified. At this time, all GEM cases are given a thorough ultrasonic inspection at the launch site just prior to attachment of the motors to the Delta core vehicle. There is a monitoring device (the IST datalogger) that is an accelerometer-based system used during the transportation of the motors from the factory to the launch site. It has been recognized, however, that no procedure can be sufficiently foolproof to guarantee that no unrecorded accidents occur. The inspection will most likely detect any fatal flaws in the case, but the inspection process is expensive, not necessarily foolproof, and it will obviously not detect any events occurring after the inspection during the mounting of the GEMs on the core vehicle. The existing monitoring system is of limited utility and is used only during transportation.

Because of these concerns, there is a strong interest in developing an advanced monitoring system capable of detecting and reporting any potentially damaging events occurring prior to launch. An ideal monitoring system would have minimal power requirements, would be wireless, would be unobtrusive when mounted on the motor case, would operate continuously from motor fabrication to launch, and would provide an absolute indication of damage to the motor, including location and magnitude of the damage. Obviously a practical system would require a compromise among these various attributes. A program was initiated at Aerospace to conduct a preliminary investigation of various elements of such a system. This report details the results of that investigation.

A monitoring system will consist of, at a minimum, a sensor that detects some physical phenomenon, and a means of transmitting information to a user. Other subsystems that would most likely be included are a power supply for operation in environments where wall power is not available, and an information processing subsystem for preliminary screening of the data. The Aerospace effort focused on sensor and information transmission aspects of the problem.

The choice of an appropriate sensor for the application is not immediately apparent. There is no such thing as a "damage sensor," so it is necessary to consider what measurable physical phenomena would be associated with a damaging impact event. Damaging impact events could fall anywhere between two extremes, one being a high-speed, low-mass event such as a wrench falling from a large height, the other being a low-speed, high-mass event such as a fork-lift backing slowly into a stationary motor. In the first case, the event will likely produce acoustic noise (audible range), noise from breaking fibers (ultrasonic), and vibrations in the form of surface waves. In the second case, very low frequency or even dc strains might be produced, along with ultrasonic noises, while audible frequency noise and vibrations are less likely. Vibrations produced at the point of impact will propagate initially as acoustic waves (compression), followed by surface waves (displacement normal to the surface). Obvious candidates for measurement therefore include noise (both low and high frequency), vibration, acceleration, and strain. Multiple sensor options are available for measurement of these phenomena, including accelerometers, acoustic emission detectors, and strain sensors. One part of the Aerospace program focused on evaluating the utility of these different types of sensors. This included a study of the propagation of acoustic and surface stress waves generated by impacts, measurements of acoustic waves and stresses caused by normal handling events, and an evaluation of the sensitivity of various sensor systems.

The second aspect of the Aerospace program dealt with data transmission. In order to collect the information necessary to detect potentially damaging events, one or more sensors will most likely need to be attached to the motor. The most complete information will be obtained if there is a system of distributed sensors deployed at numerous locations about the motor. With such a distributed system, there are a number of possible configurations for getting information about potentially damaging events to a responsible party. Data can be transmitted from the sensor nodes to one or more central collection points on the motor, and subsequently transmitted to a remote location. Alternatively, data may be transmitted directly from the sensor nodes to a remote location. None, some, or all of the data transmission pathways may be wireless. A completely wireless system will result in minimal impact on existing motor processing and handling procedures. On the other hand, a wireless system will require on-board power supplies that will need to be periodically recharged or replaced. There will also be range safety considerations associated with radio frequency (RF) transmissions in proximity to live ordinance. A wired system will eliminate concerns about power and RF transmissions, but a wired system will add concerns about direct electrical connections to wall power, and will have an impact on handling and processing procedures.

As noted above, the sensors will not directly sense damage. The acoustic, acceleration, vibration, or strain data must be analyzed to determine whether a damaging event has occurred. The data processing can occur either in real time, during post processing, or some combination of the two. The data analysis can also take place either at the sensor nodes, at a central processing location, or in some combination of the two. Distributed processing of the data increases the complexity of the sensor nodes, but decreases the bandwidth required for transmitting the information. The Aerospace effort in this area focused on evaluating wireless communication between sensor nodes and a remote receiver.

There were two test articles available for the Aerospace effort. The first test article was a segment of a motor case in approximately the same configuration as the GEM. This case, however, was not a GEM case, but was a full-scale engineering prototype that had been surplused by Alliant Techsys-

tems. Its exact configuration was unknown. We had approximately the aft 1/3 of the case, and, although the insulating liner was installed, the case was supported on soft chocks in a horizontal orientation. Experiments with this case were limited to impact events using either hand-held hammers or a calibrated pendulum impactor.

The second test article was a full-scale GEM motor filled with inert, rather than live, propellant. Most of our tests with the inert GEM took place in a warehouse at AFRL/PRR at Edwards Air Force Base. This location was selected because it provided handling and transportation services comparable to those at the launch sites, while avoiding the necessity for satisfying normal launch range safety constraints, which would have been inappropriate for an experimental program. For the impact tests, the GEM was oriented horizontally and supported on two chocks, with the inboard radius of the motor oriented vertically upward. Impact energy levels were limited to 6 ft-lb, which is below the damage threshold for the GEM case. The handling tests involved lifting the motor using an overhead crane. The motor was lifted from either end (leaving the opposite end resting on the chock), or from the center of mass (lifting the motor off both chocks). In addition to the impact and handling tests, one day was dedicated to road tests in which the motor was lifted onto a flat bed truck, strapped down in its normal transportation chocks, and driven over various roads on the AFRL site, as well as over a series of calibrated bumps. One sudden stop was performed from an initial speed of 17 mph.

The Aerospace effort was divided into five tasks, each with a different focus and a different principal investigator. The reports of each of those five tasks are presented below as five separate chapters. Each of the tasks involved applying a sensing or data handling technology to observe impact and/or handling events using one or both of two test articles available to this program. The results of each task are summarized in this section.

The first task focused on monitoring the GEM case using conventional resistance strain gages to measure the propagation of waves generated by impact events. The primary issues to be investigated were whether the strains generated by impact events would be sufficiently large to be detected, with a reasonable spacing between gages, and whether the signals could be distinguished from strain signals generated by normal handling procedures. It was observed that typical sub-damage impact events produced clearly detectable signals (greater than 20 microstrain) up to about 20 in. away from the point of impact. There were signals observed above the noise threshold (about 1–2 microstrain) over the full length of the motor case, but they were of an indistinct shape, and hard to interpret. The key observation, however, was that normal handling, such as lifting and transporting on a truck, led to signals of up to 200 microstrain, which is twice as large as a typical impact-generated signal at a distance of only 6 in. from point of impact. Clearly, a complex data analysis capability would be required to distinguish between impact events and normal handling events.

The second task focused on evaluating the utility of fiber-optic Bragg-grating sensors. The Bragg-grating sensor is another form of strain gage, and measures essentially the same phenomena as the resistance strain gages discussed in the first task. The Bragg-grating sensors have several potential advantages over the resistance strain gages: they operate through an optical fiber, eliminating the need for electrical wires to connect distributed sensors; the fiber is immune to EMI; multiple sensing elements can be included on one fiber; and the fiber can be wound into the case at manufacture, resulting in no surface changes from the current GEM configuration. The tests demonstrated that the fiber-optic system is capable of detecting signals from impact events with approximately the same

3

sensitivity as the resistance strain gages of the first task. The fiber-optic system could not be read with portable equipment, so there is no data from the road tests. However, since the fiber-optic system is measuring the same phenomena as the resistance strain gages, the fiber-optic system will be subject to the same requirements for distinguishing between impact events and normal handling events. This task also involved the development of an algorithm to triangulate on the point of impact given the arrival time of the signal at three sensors.

The third task focused on detection of impact events using accelerometers. The initial work on the empty case indicated that 50 g accelerometers had the appropriate sensitivity to detect threshold level impacts. When experiments were conducted on the inert GEM, it was discovered that the attenuation of the signal was much stronger, limiting the useful range of the sensors. Accelerometers with a 1 to 5 g maximum range would have been more appropriate. The 50 g accelerometers proved insufficiently sensitive to detect the handling events. This task also included an effort to understand the propagation of surface vibrations. In addition to anticipated anisotropies in wave propagation speeds, it was discovered that there was a significant frequency-based dispersion in wave speeds, making it difficult to triangulate the impact location without first frequency filtering the signals. When the accelerometer signals were first Fourier-filtered to eliminate everything outside the frequency band between 500 and 1000 Hz, the analysis produced consistent results for a variety of impact events.

The fourth task focused on acoustic emission monitoring. This method used piezoelectric sensors sensitive to high-frequency (>100 kHz) vibrations. In this frequency range, vibrations are produced by fiber breakage rather than bulk deformation of the solid. This task utilized a commercially available system, and demonstrated sufficient sensitivity to provide for complete coverage of the GEM case with an array of about 10 sensors. The system produced clearly identifiable signals in impact events with energies as low as 1 ft-lb. Impacts at the 6 ft-lb damage threshold tended to saturate the system. It was also observed that normal handling events, such as lifting, produced no detectable signals in the high-frequency range. The problem of distinguishing between impact and handling events is thus eliminated. The primary drawback of this system is the very high data rate required; for these tests, the data were digitized at a frequency of 5 MHz. It may be possible to significantly reduce this requirement using a parameter-based acoustic emission system, but this was not investigated in this program.

The fifth task had more of a systems focus, with the goal of demonstrating a wireless multiparameter sensor (MPS) system. In this task, a stand-alone, battery-powered MPS containing a 3-axis accelerometer, and pressure, temperature, and humidity sensors was mounted on the inert GEM. The MPS communicated by wireless modem with a portable computer. The prototype system successfully detected impact events, and recorded temperature, barometric pressure, and humidity with a high degree of precision throughout the day of the tests. This demonstrated the capability for wireless environmental monitoring and, in principle, demonstrated the capability for wireless detection of impact events using accelerometers. The MPS is configured to allow inputs from additional sensors, and the extension to a distributed array of accelerometers (or a distributed array of another type of sensor) is straightforward. This task also included an investigation of the reliability of wireless data transmission. In the warehouse at AFRL, the maximum data rate for communication between the MPS and the receiving computer ranged between 200 and 400 kb/s, depending on location of the receiver in the warehouse.

This program has produced a series of results that demonstrate some key technologies leading to the development of a comprehensive health monitoring system for solid rocket motor cases. This program has also allowed us to identify some key issues that will need to be resolved in order to build such a monitoring system. Several key results will help provide a framework within which the specifications for any new deployable monitoring system can be developed. These results can be summarized as follows:

1. The speed of propagation of acoustic waves is strongly anisotropic, with propagation speeds being higher along fiber directions. Measured speeds ranged from 180 to 440 m/s.

2. There is significant dispersion in the wave speeds, with the higher frequency waves traveling faster. This made it difficult to determine wave speed by noting only the arrival time of the signal from an impact event.

3. The attenuation of the acoustic waves in the filled motor case was substantially higher than in the empty case. Sensor systems determined to be adequate for the empty case were often found not to be sufficiently sensitive for the filled case.

4. At the threshold for impact damage, the fiber optic and conventional strain gages yielded similar results on the filled motor, with a peak value of about 15 micro-strain at about 0.5 m from the point of impact. The signal strength decayed exponentially with distance, making it difficult to pinpoint the arrival time of any event originating more than one meter from the sensor location.

5. The lifting exercises produced strain signals of 200 to 500 micro-strain, which is much larger than the impact-generated strain signals.

6. The strapping of the motor to the truck bed also imposed a significant strain offset (80 micro-strain) to the dynamic signal monitoring.

7. Running the truck at 15 mph over a series of wood 2 x 4s produced dynamic strain oscillations of ±100 micro-strain with a nominal bandwidth of 10 Hz. This large dynamic background signal would make it difficult to separate an impact strain signal from a "transportation and handling" signal.

8. With the Acoustic Emission (AE) technique, impacts of 1 ft-lb were readily detected at distances of 1 m. Impacts at the damage threshold (6 ft-lb) were detectable at distances of up to 3 m. While AE was sensitive to impact events, it was insensitive to normal handling procedures allowing AE to monitor for impacts during normal operations without a loss in sensitivity due to signal masking.

9. The useful data rates obtainable with the wireless system varied from 100 kb/s to as high as 405 kb/s depending on the position in the warehouse, the orientation of the antennas, and distance from the booster. This could support the accelerometer or strain sensor systems without any on-board processing. Wireless support of the acoustic emission

5

system would require on-board processing to detect and analyze impact events before the information about the events is transmitted wirelessly.

The results of these experiments demonstrate that there are no fundamental technical roadblocks that would prevent the development of a useful health monitoring system for composite solid rocket motor cases. Future work should focus on selecting and optimizing a sensor technology, and evaluating and resolving the operational issues that will be encountered in attempting to field a monitoring system. Continuation of this work, leading to a successful development and deployment of a reliable health monitoring system for solid rocket motors could have a significant positive impact on launch operations and launch system reliability. Natural extensions of the techniques developed under this program will lead to health monitoring capabilities for many other launch-related systems, eventually leading to development of an overall "smart launch base," with significant improvements in reliability and operability compared to current systems.

2. Impact Monitoring and Reference Strain Measurement Using Conventional Resistance Strain Gages (L. H. Wiedeman)

2.1   Abstract

A series of low-energy impacts (below damage threshold) were monitored on subject graphite/epoxy motor cases using conventional strain gages. Similar impact tests were done on an empty case and a Delta GEM inert-propellant-loaded case. The conventional strain gages were also used to monitor case bending during lifting, handling, and transportation shock exercises. The impact test energies ranged between 1 and 6 ft-lb with a 5/8-in. tup. The 6 ft-lb impacts impart a sufficiently large strain wave to be sensed by all gages on the inert loaded motor, regardless of location or orientation. This includes impacts on the cork covering. However, the strain signals for some of the remote impacts are pushing the lower limit of detection for this system (1 microstrain). Typical strains measured for a 6 ft-lb impact on the inert-loaded case were 15 microstrain when the gage was located 17 in. from the impact. The strain impulse damping with distance is roughly exponential for the sharp impulse and very slight for the lower frequency ringing. The strain waves have remarkably reproducible amplitudes and shapes for successive impacts at a given location and energy. However, the recorded waves are dependent on factors such as the orientation of the gage with respect to the case (axial vs. circumferential), the mode and direction of the wave propagation, and the location of the impact. These factors make it difficult to predict the exact wave shape for an arbitrary combination of impact location and gage orientation. The lifting exercises produced strain signals of 200 to 500 microstrain, which is much larger than the impact strain signals. The strapping of the motor to the truck bed also imposed a significant strain offset (80 microstrain) to the dynamic signal monitoring. Running the truck over a series of wood 2 x 4s produced dynamic strain oscillations of ±100 microstrain with a nominal bandwidth of 10 Hz. This large dynamic background signal would make it difficult to separate an impact strain signal from a "transportation and handling" signal.

2.2   Experimental

The reference strain measurements were made with standard laboratory equipment. The ensemble included Micro-Measurements rosette gages (P/N CEA-00-250UR-350) bonded to the case with M-Bond AE-10, and a Micro-Measurement 3110 strain gage signal conditioner amplifier. The signal conditioner was typically set to 10 V excitation drive, 10,000 gain, 10-kHz band-pass filter, and wired as a 1/4 bridge circuit using the internal 350-ohm resistors. For this experiment, unshielded cable was used successfully. However, this is not recommended since it is vulnerable to picking up RF noise from a host of uncharacterized sources. Three independent, 3110 signal conditioners were used in parallel to simultaneously drive the three gages on the rosette. The output signals were recorded at 8,000 points/s along with the output from a load cell located between the impact tup and the dead-weight of the pendulum impactor. A circular data acquisition buffer was used to allow pre-trigger data to be included with each impact waveform. The data was digitized with a National Instruments MXIO-16F card and driven with "C" code running on a 486, 33-MHz desktop computer. The

impact locations were chosen in an attempt to de-couple axial vs. circumferential wave propagation. A listing of the impacts can be found in Table 2-1, and a visual reference is provided by the experimental map. Points #3 and #12 were chosen as "maximum distance from the gage" impact points. All plots include a short section (negative time) of "pre-impact" points to show the baseline signal-to-noise limit.

Table 2-1. Impact Location and File Number Reference

Test No.	Location Map	Strain Gage and File No.	Impact energy (ft-lb)	Remarks	Impactor X location (in.)	Impactor Y location (in.)
0	NA	B 001	< 1	Background	NA	NA
1	1	B 002	6	Left Side	-42.625	30.5
2	1	B 003	6		-43.125	30.5
3	1	B 004	6	Fiber breakage observed	-42.25	30.5
4	1	B 005	6	Crack above the impact spot	-42.25	30.5
5	1	B 006	3		-40.94	30.5
6	1	B 007	3		-40.94	30.5
7	1	B 008	3		-40.25	30.5
8	1	B 009	1		-39.75	30.5
9	1	B 010	1		-40	30.5
10	1	B 011	1		-40	30.5
11	2	B 012	1		-34	30.5
12	2	B 013	1		-34	30.5
13	2	B 014	1		-35	30.5
14	2	B 015	3		-34.375	30.5
15	2	B 016	3		-33.625	30.5
16	2	B 017	3		-33.75	30.5
17	2	B 018	6		-33.5	30.5
18	2	B 019	6	Fiber breakage observed	-33.5	30.5
19	2	B 020	6		-31.5	30.5
20	3	B 021	6	Right Side	122.75	-30.5
21	3	B 022	6		122.25	-30.5
22	3	B 023	6		121.125	-30.5
23	3	B 024	3		120.1875	-30.5
24	4	NA	3		73.375	-30.5
25	4	NA	3		73.5	-30.5
26	4	NA	3		72.75	-30.5
27	4	NA	6		73.5	-30.5
28	4	NA	6		72.25	-30.5
29	4	NA	6		71.5	-30.5
30	5	A 025	6	Cork	81.375	-30.5

Test No.	Location Map	Strain Gage and File No.	Impact energy (ft-lb)	Remarks	Impactor X location (in.)	Impactor Y location (in.)
31	5	A 026	6	Cork	81.375	-30.5
32	5	A 027	6	Cork	80.375	-30.5
33	6	A 028	6		21.375	-30.5
34	6	A 029	6		21	-30.5
35	6	A 030	6		20.25	-30.5
36	6	A 031	3		19.25	-30.5
37	6	A 032	3		19	-30.5
38	6	A 033	3		18.5	-30.5
39	7	A 034	3		-71.125	-30.5
40	7	A 035	3		-70.25	-30.5
41	7	A 036	3		-69.625	-30.5
42	7	A 037	6		-74.188	-30.5
43	7	A 038	6		-74.75	-30.5
44	7	A 039	6		-74.188	-30.5
45	8	A 040	3	Left Side	-40	30.5
46	8	A 041	3		-41	30.5
47	8	A 042	3		-41.375	30.5
48	8	NA	3		-39.125	30.5
49	9	A 043	3		16.25	30.5
50	9	A 044	3		16.5	30.5
51	9	A 045	3		17	30.5
52	9	A 046	1		17.75	30.5
53	9	A 047	1		17.625	30.5
54	9	A 048	1		16.875	30.5
55	9	A 049	3		14.5	30.5
56	9	A 050	3		15.5	30.5
57	9	A 051	3		14.125	30.5
58	9	A 052	3		15	30.5
59	9	A 053	6		14.125	30.5
60	9	A 054	6		14	30.5
61	9	A 055	6		15.25	30.5
62	10	A 056	3		51.25	30.5
63	10	A 057	3		51.125	30.5
64	10	A 058	3		51.375	30.5
65	10	A 059	6		52.25	30.5
66	10	A 060	6		52	30.5
67	10	A 061	6		52.375	30.5
68	11	A 062	3		61.625	30.5
69	11	A 063	3		60.875	30.5
70	11	A 064	3		61.375	30.5
71	11	NA	3		61.875	30.5
72	11	NA	3		62.5	30.5

Test No.	Location Map	Strain Gage and File No.	Impact energy (ft-lb)	Remarks	Impactor X location (in.)	Impactor Y location (in.)
73	11	A 065	6		62	30.5
74	11	A 066	6		63.25	30.5
75	11	A 067	6		63.5	30.5
76	12	A 068	6	Extreme Tail	-176.5	30.5
77	12	A 069	6		-176.5	30.5
78	12	A 070	6		-175.5	30.5
79	12	NA	6		-175	30.5
80	12	NA	6		-174.75	30.5
81	12	NA	6		-174.75	30.5

The experimental map (see Figure 2-1) splits the motor into sides—top, bottom, left, and right (bottom side not plotted). With the motor on the chocks, the nozzle is angled towards the ground, and this defines the bottom. Since the impactor hits the midline of the case, all impact points are in the center of either the left or right side. All dimensions and distances are inches measured along the surface. The three gages within one rosette are defined in terms of their orientation. The "X" gage is along the axial direction, the "L" gage is parallel to the circumferential direction and the "XL" gage is oriented at 45° to both the axial and circumferential axes. Included in the table are the impact positions for which strain gage waveform data were recorded, the data file name and the gage used. Although not presented, the data are available for further analysis, and, in many cases, comparable impact strain data were also recorded on the empty case.
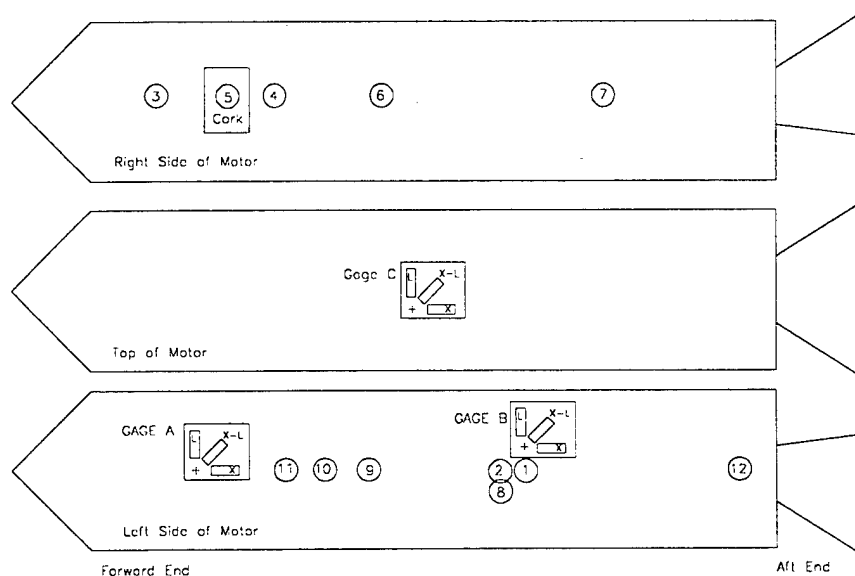

Figure 2-1. Experimental map. Relative location of gages and impacts.

2.3   Data and Results

Figure 2-2 shows three representative strain waveforms from one location and three different energies. These data are from impact location 1, and the data are from gage B-L. This gage is located along a circumferential line, 17 in. from the impact. Although data were recorded from all three gages on the rosette, only the gage line aligned with the impact spot to gage centerline is presented in this plot. The three impact energies are nominally 1, 3, and 6 ft-lb. The impact force was measured simultaneously and recorded with the strain data. The data show essentially a single, sharp impulse followed up by much lower amplitude, low-frequency ringing. The structure of both the strain impulse and the low-frequency ringing is extremely reproducible. Multiple impacts were made at each energy, and the shot-to-shot wave shapes are virtually identical. The wave shape does not change with increasing impact energy, and the peak height scales roughly linearly with impact energy. Impact energies above 7 ft-lb are expected to cause damage to the case. For this reason, 6 ft-lb was the maximum impact energy used. One would expect the wave shape to change with impact energies above the case damage threshold and to see a sublinear increase in amplitude. The wave shapes from the three different gages on the rosette (not presented) are all visually distinctive from each other, and reproducible. Interpretation of the waveforms is beyond the scope of this report.

Figure 2-3 re-plots the 3 ft-lb impact waveform from Figure 2 at an extended time scale along with a representative strain wave from an impact on the empty case. This empty case impact was nominally 3 ft-lb, and the impact gage geometry is fairly close to the inert loaded case, gage B-L, impact location 1. All of the empty case waveforms are much larger in amplitude than the loaded case waveforms and extremely complex. For the empty case, the waveform fine structure is very reproducible, and the signals from each gage on the rosette have distinctive fingerprints. These strain waves appear to be damped ringing waveforms with frequency components nominally within the 50 to 200
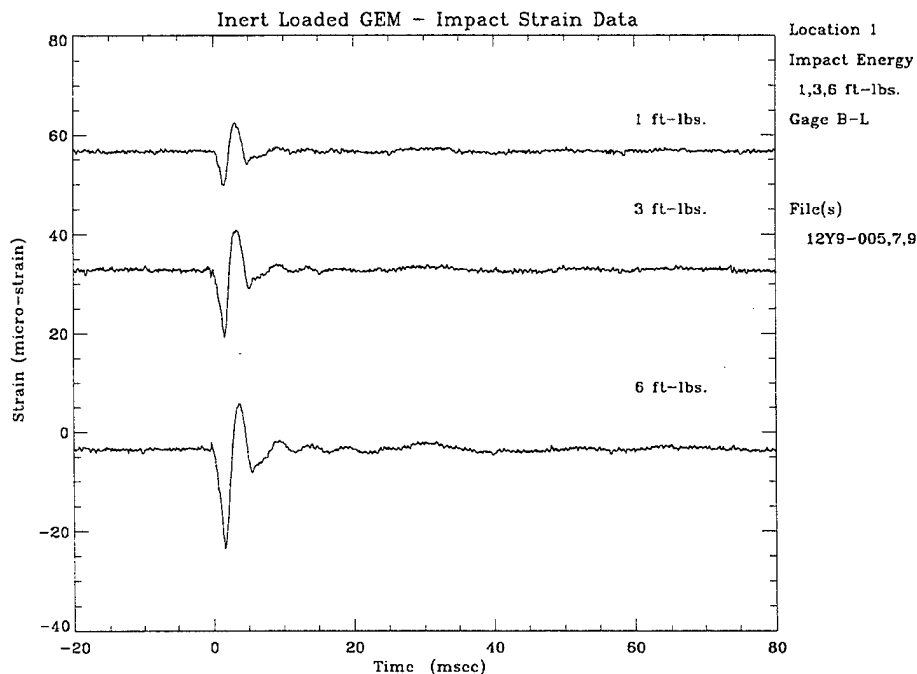
Figure 2-2. Strain impulse for three different impact energies.
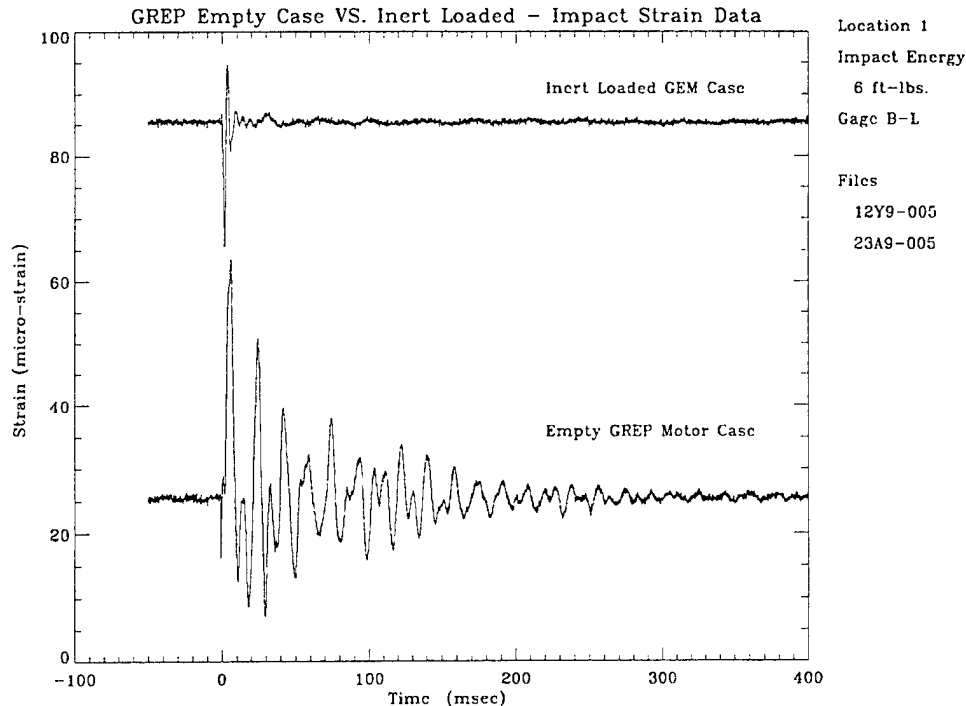
Figure 2-3. Comparison of strain waves propagated in an empty case and the inert-propellant-loaded GEM.

Hz range. This shows that one cannot predict the Gr/Ep surface impact strain signatures based on empty case impact data without a rigorous understanding of the overall mechanical structure.

An attempt was made to measure the damping of the waveform in the loaded GEM as the impact is axially removed from the strain gage. Figure 2-4 shows impacts at 6 ft-lb for four different axial distances from the gage. The data presented are only from gage A-X. This gage was oriented parallel to the motor axial dimension and the located near the center of the motor's left side. This provides for a linear-axial wave propagation path (from several impacts to the gage) without a circumferential component. The top trace impact is 6 in. from the gage. The next trace down is at 17 in. from the gage, and the impulse spike is about 1/4 of the amplitude of the top trace. The third trace is 52 in. from the gage, and the impulse spike is virtually gone. The lower frequency ringing component is not damped nearly as much as the sharp impulse spike. This is more obvious when the data are plotted out to the full 800 ms. The bottom trace is from an impact near the tail of the motor, 243 in. from the gage. The amplitude of this trace is about half that from an impact 20% of this distance from the gage. Only the top two plots have sufficiently well-defined impulse spikes for wave propagation time measurements. The relative peak separation is too small in relation to the peak widths and the width of the impact impulse to make an accurate measurement of the wave velocity.

Figure 2-5 is a semi-random collection of waveforms from impacts geometrically removed from the sensing gage (i.e., impacts on the other side of the motor case). This plot is extended out to 400 ms since there are no impulse spikes observed, and the longer time plot better shows the low-amplitude ringing. The top trace is from a 6 ft-lb impact at location 3, gage B-L. With the exception of the tail hit, this was the farthest removed (210 linear inches) impact-to-strain-gage combination tested. This

12

Figure 2-4. Axial strain wave propagation at different gage-to-impact distances.
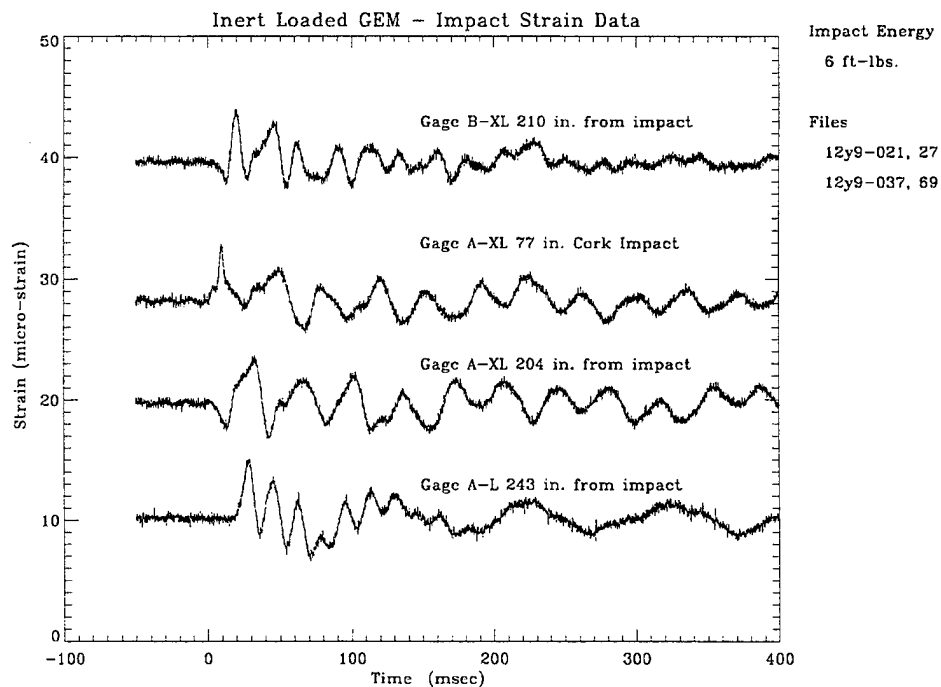
Figure 2-5.   Assortment of strain waves from different impact - gage geometrical combinations.

13

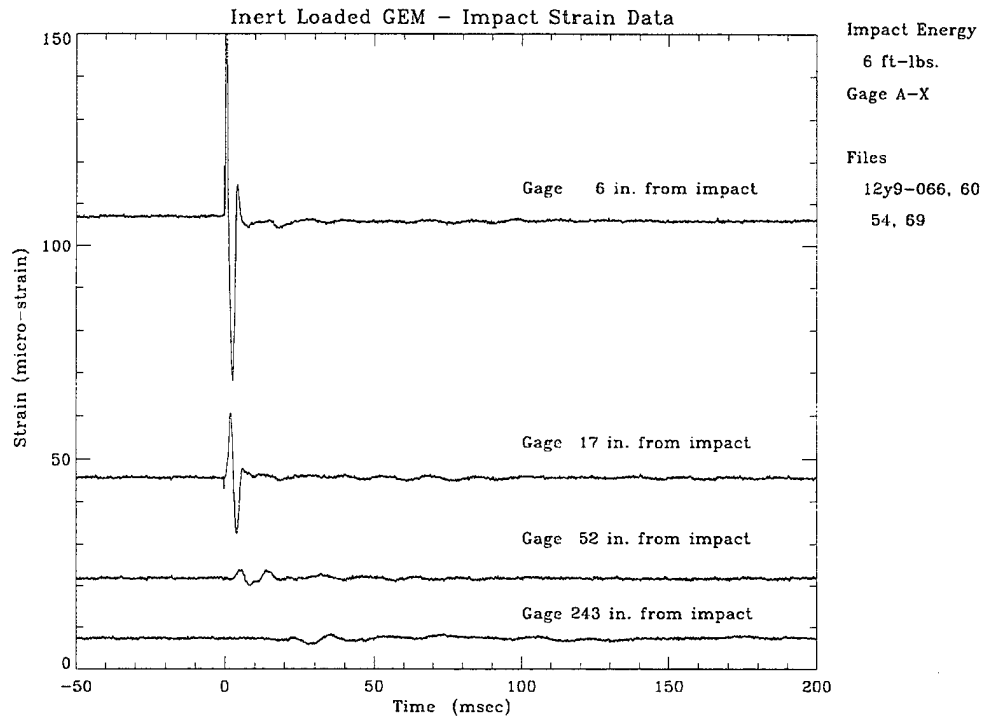impact-to-gage distance is roughly comparable to the maximum possible gage-impact distance, assuming one were to mount a single gage at the motor midline. A 3 ft-lb impact was also recorded for this impact-gage location and the signal was still above the noise floor. The middle trace is from a 6 ft-lb impact at location 5 (hitting on the cork), a distance of 77 in. from the gage and recorded with gage A-LX. The next trace (second from bottom) is from a 6 ft-lb impact location 7, gage A-LX. This impact is a net linear distance of 204 in. from the impact to the gage. The bottom trace is another "tail hit" wave form, monitored with gage A-L and an impact distance of 243 in.

Lifting, handling, and transportation strain signals were also monitored. Any attempt to extract impact data from dynamic strain measurements needs to be able to separate impact signals from background transportation and handling strains. A third strain gage (gage C) was located at the top center of the motor case for measuring the maximum strains with various lifting stresses. A maximum axial strain difference of 500 microstrain was measured from the motor at rest in the chocks to a single-point lift at the center of the motor. This strain is huge relative to the ±10 microstrain signals from the impacts. Furthermore, dynamic strain oscillations of ±25 microstrain were recorded when the motor was set back into the chocks from a lift position. A background strain of 80 microstrain was recorded when the motor case was tied down to a flatbed truck with ratchet straps. The ratchet straps typically "pop" when released. This would probably cause a large strain impulse to be launched into the motor. An attempt to record this impulse was made. However, the trigger timing was not successfully coordinated and no results are available.

Road strains were recorded by driving the loaded flat-bed over a set of wood 2 x 4s at approximately 15 mph. Figure 2-6 shows a very dynamic, oscillating strain signal induced by the 2 x 4 bumps. The peak amplitudes are ±150 microstrain with a frequency of about 10 Hz. Also shown in the figure is a
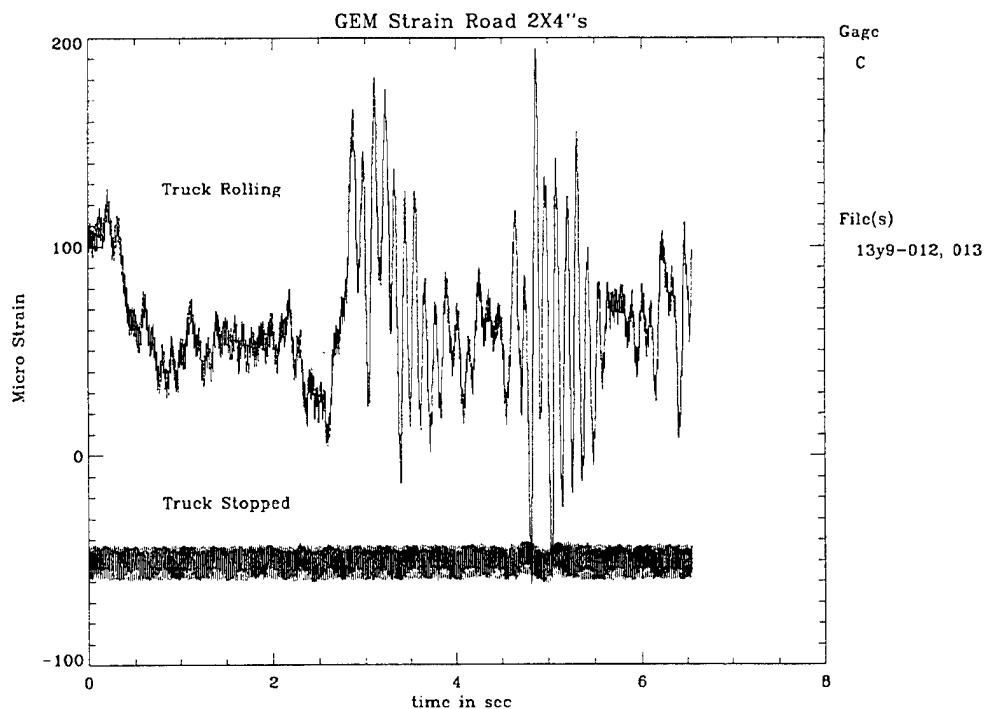
Figure 2-6. Log of GEM strain during transportation and running over a wood 2 x 4.

trace with the truck stopped, but still running. The high background noise is believed to be rf coupled into the first-stage pre-amplifier from a nearby DC-to-AC converter. This rf noise problem was much worse before including a 100-Hz low-pass filter on the signal line.

2.4   Discussion

At impact energies below damage threshold, very reproducible strain waves and impulses are launched into the Gr/Ep motor cases. These strain waves are relatively large in magnitude and can be easily sensed by conventional resistance strain gages located fairly far from the impact location. The sharp impulse signal magnitudes track reliably with impact energy, and the low-frequency ring-down signals that follow the impulses are distinctive and reproducible. However, predicting these signatures, especially in view of the dramatic difference between the empty case and the inert loaded case, would require a very sophisticated understanding of the Gr/Ep case-propellant structure. Other parameters such as impactor geometry, impact angle, etc. are also expected to change the waveform signatures.

The background strains from lifting, handling, and transportation were large relative to the impact strain signals. This could make impact identification and waveform interpretation difficult under non-static conditions. Presumably, the road-bump, flat-bed truck transportation environment used in this test series is much more severe than the flight GEMs are subjected to. The data do serve to illustrate the inherent difficulty of separating a small fast transient from large non-static signals.

There is the potential to extract more information from this dataset. Power spectral density analysis of the impact waves or motor flexing with road bumps may be of value. This is, however, beyond the scope of this report. A large set of "empty case" impact data also exists. The digital data, along with a digitized signal from a load cell on the deadweight impactor are available on request.

3. Impact Sensing with Fiber-Optic Bragg Grating Sensors (C. M. Klimcak, Y. Chan)

3.1   Introduction

A full-scale Delta II inert graphite/epoxy solid rocket motor (GEM) was instrumented with fiber-optic Bragg grating strain gages in order to assess the feasibility of developing a GEM impact monitoring system with EMI-immune fiber optic sensors. Such a system could potentially be used to determine the location and magnitude of an inadvertent impact to the solid rocket motor during its handling and transportation. Data regarding the impact would be derived from an analysis of impact-produced strain transients that are detected with an array of fiber optic sensors that is distributed over the surface of the motor. Specifically, the impact energy would be obtained from the peak magnitude of the strain transient, and the location of the impact would be computed from measurements of the arrival times of the transients at several sensors using standard triangulation methods. This knowledge could permit an assessment of the effect of the impact on the structural health of the motor, as well identify the specific areas on the motor that should be subjected to further non-destructive evaluation.

3.2   Experimental

Three fiber-optic Bragg grating sensors manufactured by Electrophotonics Corporation for use with an Electrophotonics FLS 3100 fiber-optic strain sensing control unit were bonded to the cleaned surface of the inert motor using polycyanoacrylate cement. All of these sensors were aligned with the fiber and grating directions parallel to the circumferential direction (i.e., transverse to the cylindrical axis of the motor). The sensors were bonded in a triangular pattern onto the surface of the motor at the following (X, Y) coordinates: (3.64, 0.44), (4.14, 0.84), and (4.64, 0.44). In this coordinate system, the dimensions are in meters, and the origin of the coordinate system is located at a point on the graphite/epoxy casing that is immediately adjacent to the nose cone and at the radial location that would be closest to the core vehicle if the GEM were mounted. The X axis is measured along the axis of the GEM, and the Y axis is measured around the circumference.

The FLS 3100 strain sensing unit is a calibrated device that produces a voltage that can be converted to strain using a vendor-supplied calibration curve and constants. This unit had a strain resolution of 1 microstrain and a bandwidth of 1 kHz. It was equipped with three plug-in units, permitting simultaneous detection of strain transients from each of the three Bragg sensors. The analog outputs from these units were digitized with three channels from a Tektronix TDS 455A four-channel digital oscilloscope and stored on disk. The fourth channel was used to acquire impulse data from load cells associated with either a handheld impact hammer or a calibrated pendulum impactor. This load cell output voltage was also used to trigger signal acquisition. In most cases, a total record length less than 20 ms was employed, restricting acquisition to only the fast transient response. For some experiments, we employed a laboratory-built sensor demodulator instead of the FLS 3100 unit to achieve higher sensitivity. This demodulator utilized Bragg receiver gratings to convert the temporal

wavelength shifts of the sensor gratings to an intensity transient proportional to the instantaneous strain.

A 3-lb hand-held hammer having a flat 2-in.-dia hard plastic head was used to impact the motor at several different locations while recording the strain transients from each of the sensors. The impulses were typically ≈0.5 ms in duration with a peak force up to 2000 lb. This data was used to examine the dependence of the response waveform on the distance between the sensor and the impact location, and to determine propagation velocities and their anisotropy. We observed considerable damping of the fast transient response, necessitating the use of signal-averaging techniques to improve the signal-to-noise ratio. Synchronization of multiple impacts was assured by triggering acquisitions with the load cell output.

We also performed measurements at a single point with a pendulum impactor having a 5/8-in. tup and an impact energy of 6 ft-lb at the coordinate location (3.6, 0.8). This test was performed to permit a comparison of the fiber strain response to that of conventional bonded foil strain gages.

Several lifting tests were also performed in which we recorded the change of strain at one of the sensor positions induced by lifting. The Bragg receiver grating demodulator was used for these tests in order to be able to offset the preamplifier and use the highest gain to achieve maximum sensitivity.

3.3   Results

Typically observed transient signals are shown in Figures 3-1 and 3-2 for impact locations that were increasingly distant from the sensor. The shape of the transient signal and its phase was found to be dependent upon the relative angular orientation between the Bragg grating direction and the line that connects the sensor and the impact location. This can be seen by comparing the 2nd trace from the top
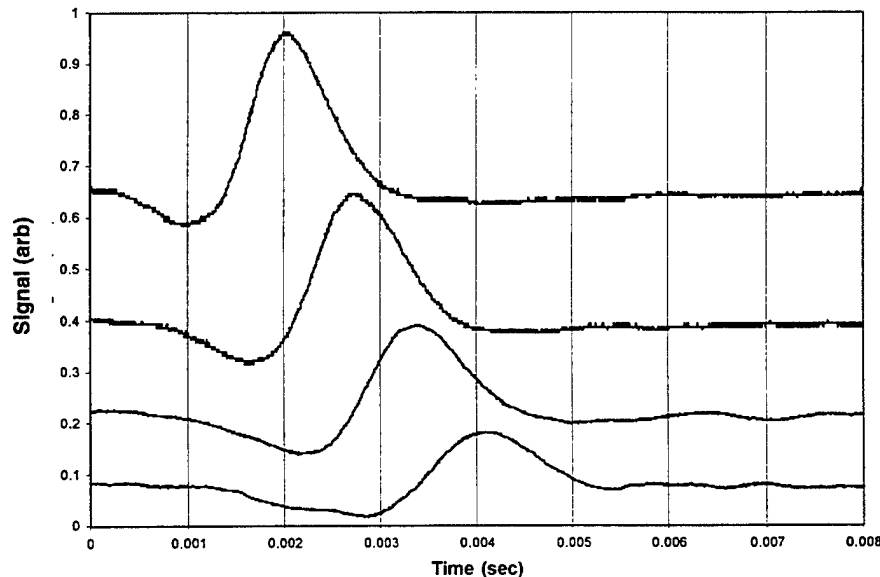
Figure 3-1. Observed impact-induced transient strain signals from one Bragg sensor. Impacts from top to bottom are at distances of 12.5, 25, 37.5, and 50 cm from the sensor.

18
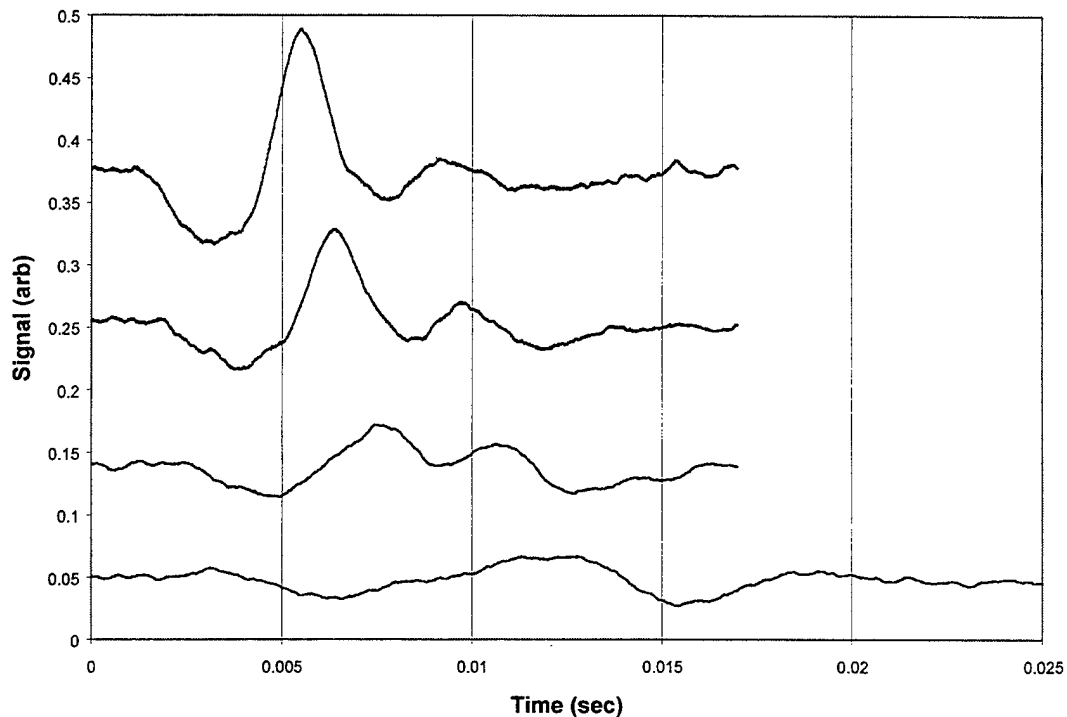
Figure 3-2. Observed impact-induced transient strain signals from one Bragg sensor. Impacts
from top to bottom are at distances of 75, 95, 123.5, and 173.5 cm from the sensor.
Note the vertical and horizontal scale changes relative to Figure 3-1.

of Figure 3-1 with that in Figure 3-3. Consequently, when directly comparing the signals acquired
from different locations, it was necessary to ensure that all impact locations fell on the same line to
the sensor.

At a few locations, we measured strain responses as a function of applied impact force. This data
showed that the peak strain signal was linearly proportional to the force of the impact over a range of
a factor of 5 in applied force, indicating that the peak strain was a good estimator of impact force.
(We have not considered whether this linearity will hold if the nature of the impactor is changed, e.g.,
hard vs. soft, round vs. flat, high vs. low mass, etc.) Measurements were then taken at different dis-
tances from a single sensor to determine the degree of damping in the motor casing. We found that
the normalized peak strain signal (i.e., the peak strain per unit applied force) exhibited an exponential
damping length of approximately 40 cm, as shown in Figure 3-4. That is, the peak strain response
declined by 1/e when the impact location was shifted by 40 cm along the line formed by the sensor
and the previous impact point. The maximum sensor separation will be critically dependent upon this
damping length due to possible dynamic range limitations. Operation will very likely be restricted to
a maximum of 4–5 damping lengths (i.e., signal ratios of 50 to 150) corresponding to a sensor sepa-
ration of 1.6–2 m.

19
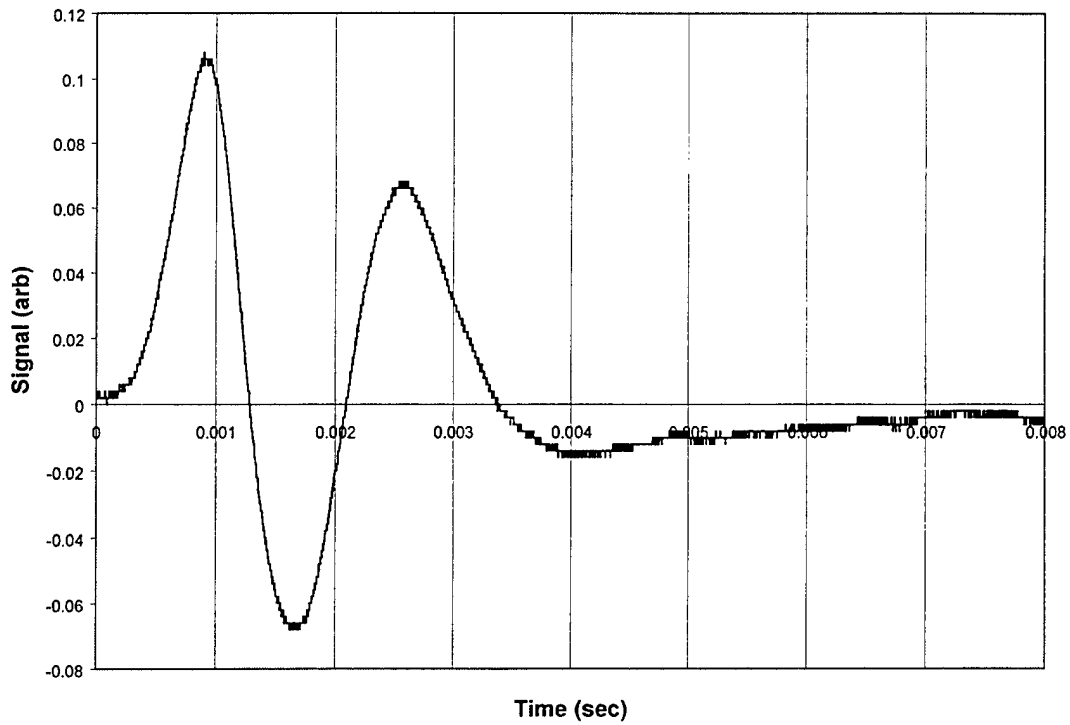
Figure 3-3. Observed strain signal from one Bragg sensor at a distance of 20 cm from the sensor along the direction of the fiber. The line between the sensor and the impact location used to produce this signal is perpendicular to that used to produce the signals in Figure 3-1.
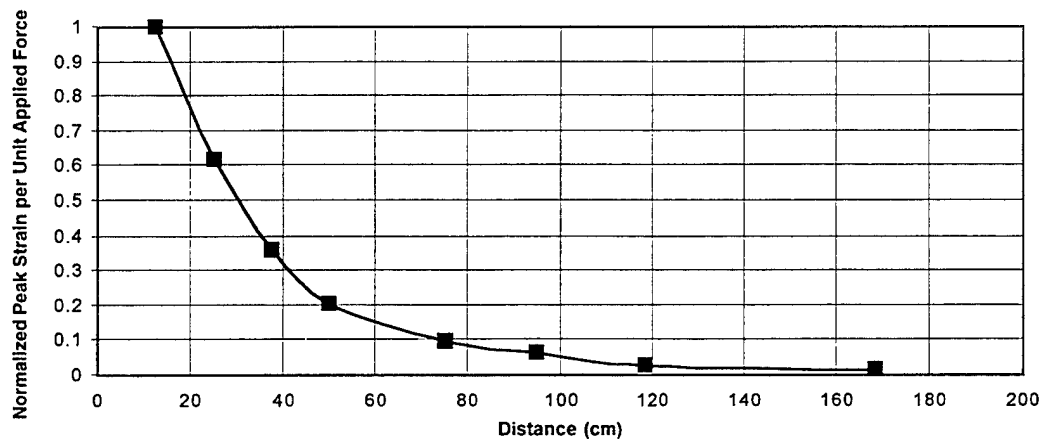
Figure 3-4. Distance-dependent damping of the impact. The 1/e damping length is ≈40 cm.

Recorded transient waveforms were analyzed using a moment analysis technique that enabled us to determine group wave velocities. This was necessary to account for the dispersion effects that occurred at distances larger than 50 cm from the sensor. In this method, a normalized first moment t_m was defined as follows:

$$t_m = \frac{\int t(S(t))^2 dt}{\int (S(t))^2 dt},$$

where S(t) is the recorded transient strain waveform. A set of normalized moments were then computed as a function of the upper integration limit, and then they were plotted versus the integration limit. In most cases, these plots exhibited a step-like appearance, and the step or plateau level of the plot was taken to be equal to the group arrival time of the transient. For example, this is illustrated by the graph in Figure 3-5 from which a group arrival time of 0.12 s was determined . This method was then used to determine the arrival times of the transient signals resulting from several impacts along directions parallel (longitudinal) and perpendicular (transverse) to the axis of the motor, and the corresponding propagation velocities were computed. A parallel velocity component of 249 ± 10 m/s and a perpendicular component of 181 ± 6 m/s were found. The results are plotted in Figures 3-6 and 3-7. To be certain that the moment analysis method was not introducing errors, the propagation velocities were computed for impacts along the longitudinal axis using a method based on the 1st zero crossing of the transient response. The results are shown in Figure 3-8. This method produced a longitudinal velocity of 220 ± 17 m/s, a value that was in reasonably good agreement with the moment method.

Using these velocities and an anisotropic model of wavefront propagation, we compared the theoretical arrival times of a series of impacts to actual measured values for impacts at random positions and angles to the sensors. Discrepancies between computed and measured arrival times were converted to distance errors using the average velocity. We obtained an average distance estimation error of 14 ± 15 cm.
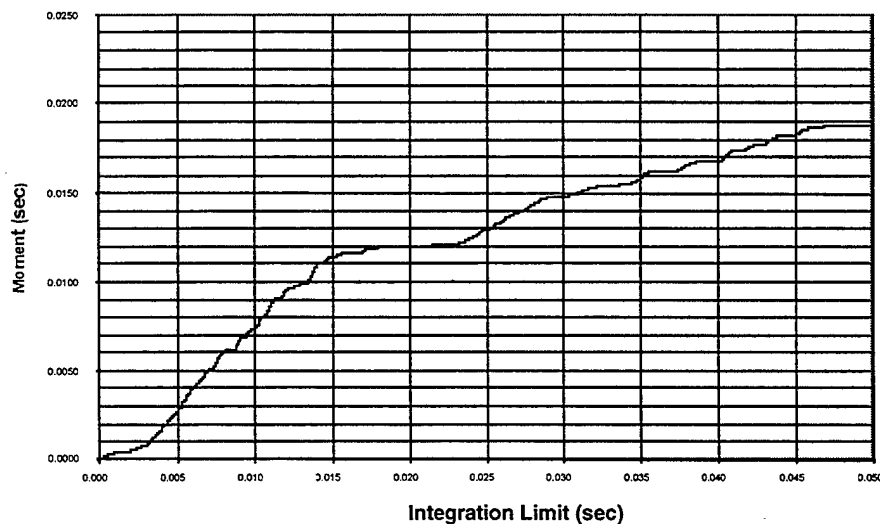
Figure 3-5. Graphical representation of moment calculation. The moment (in units of seconds) is plotted on the ordinate versus the integration limit (also in units of seconds). From this graph, we have determined a group arrival time of 0.012 s.
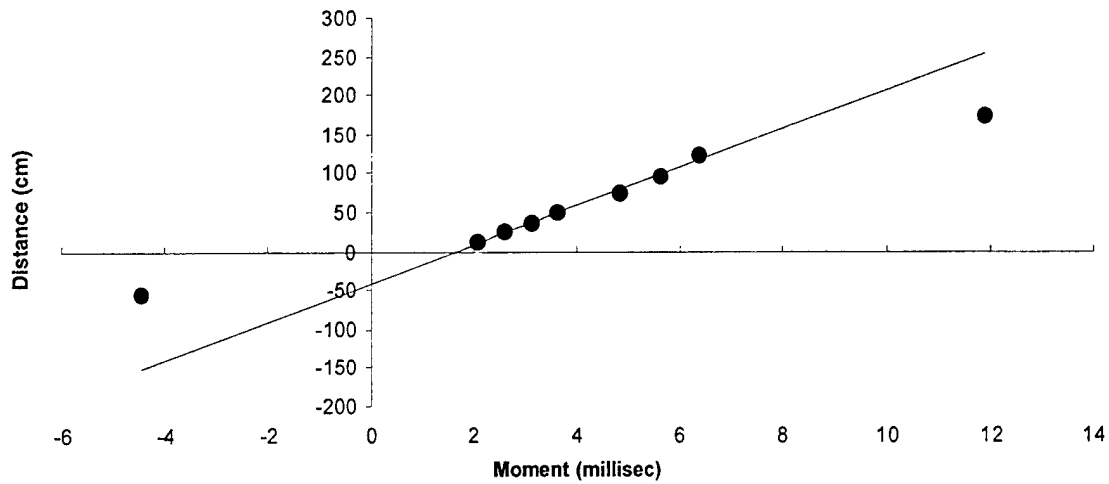
Figure 3-6. Longitudinal impact data computed using the moment analysis method.
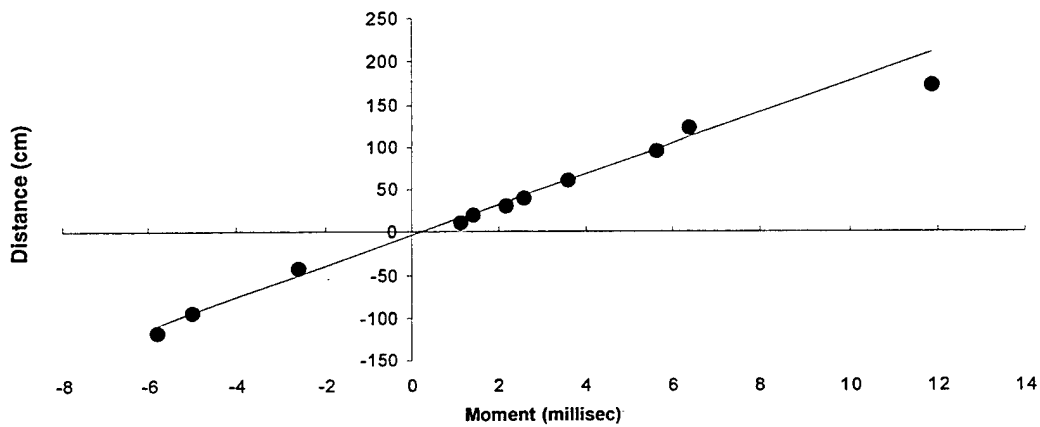
Figure 3-7. Transverse impact data computed using the moment analysis method.
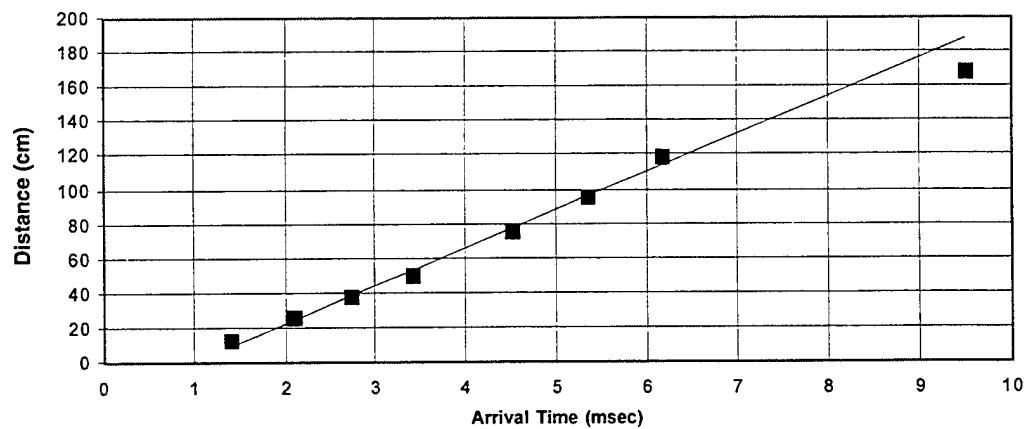
Figure 3-8. Longitudinal impact data computed using the zero-crossing method.

22

In addition to conducting measurements with the commercial Electrophotonics fiber-optic strain sensing unit, we also employed a laboratory-built Bragg receiver grating-based sensor demodulator. This unit had 3 times greater sensitivity than the Electrophotonics control unit but was not as readily calibrated for measuring strain. This unit had been previously tested with a laboratory-scale impact demonstration and found to perform quite satisfactorily. It likewise performed well on the full-scale motor and was used during the lifting measurements. These measurements have not yet been calibrated and will be reported later.

A pendulum impactor measurement was also performed to permit comparison of the fiber-optic sensor performance with that of conventional bonded foil strain gages. Unfortunately, the bonded foil gages were not co-located with the fiber-optic sensors, preventing an exact comparison. Nevertheless, a 6 ft-lb pendulum impact at a position 21 in. from a fiber sensor produced a peak strain change of 11 microstrain compared to an impact 17 in. from a bonded foil gage that yielded a peak strain of 15 microstrain. This agreement is good, particularly after one scales for the relative damping effects at the two distances.

3.4   Conclusions

This experimental study indicates that a distributed Bragg-grating-based fiber-optic strain sensor system could be developed for the measurement of the location and intensity of impacts to the Delta II graphite/epoxy motor. The principal technical challenge is the development of a Bragg-grating demodulator that possesses the dynamic range and sensitivity required to detect threshold level impacts at a distance of 2 m. The sensitivity of the present commercial system (Electrophotonics FLS 3100) was only adequate for detecting single-shot, near-threshold impacts at a distance of ≈ 0.5 m, slightly larger than one damping length. These impacts were detected with a localization accuracy of 0.15 m. A laboratory-built Bragg demodulator improved performance by about 1 damping length, but further improvement is required to be able to detect impacts and determine their location and magnitude with a manageable number of sensors (<20).

Accurate localization of the impact and determination of its magnitude is critically dependent upon achieving this improved performance. An additional factor of 16 increase in sensitivity would be required to extend detection out to a distance of 2 m, requiring enough dynamic range for signals differing by less than a factor of 150. Improved signal processing should permit realization of this goal. Possible improvements include the use of phase-sensitive signal processing with intensity modulation in the MHz regime to reduce low-frequency electronic noise, the use of higher power light sources, and the use of narrower bandwidth Bragg sensor and receiver gratings. Additionally, the power spectral density of the impact may significantly affect the ability to develop an effective localization algorithm, a possibility that was not closely examined in this investigation. If so, the use of advanced signal processing algorithms (e.g., Fourier techniques, neural networks) may be required.

4. Measurements of Acceleration on Delta GEM Boosters
(S. T. Amimoto, D. J. Chang, E. W. Fournier, E. M. Yohnsee)

4.1   Introduction

This section documents the efforts using accelerometers as a means to monitor the status of the Delta II GEM motor casings. The vibrational and wave propagation characteristics of the empty booster case at Aerospace and the inert-filled booster at AFRL/Edwards were measured using a suite of accelerometers. The sensor suite consisted of five physically distinct sensors. Two sensors used dual, longitudinal- and latitudinal-sensing accelerometers. The remaining three were single-axis accelerometers oriented in the longitudinal direction. The objectives of this study were to develop a methodology to measure wave speeds on the cylindrical casing and to triangulate impact locations over large distances. Data were also taken for impact tests and for the road tests, but are inconclusive due to the use of insensitive accelerometers.

4.2   Experimental Methods

Wave speed data were acquired using a set of two-axis 50-g accelerometers oriented in the circumferential and longitudinal booster directions. The accelerometers were first placed along the top azimuth of the empty, horizontally positioned motor case located in Bldg. 130, SMC/LAAFB. The locations of the longitudinally aligned accelerometers were (50, 0), (100, 0), (150, 0), and (200, 0). The sensor locations for the circumferentially aligned accelerometers were (50, 0), (50, 35), (50, 70), and (50, 105). The dimensional unit is cm. The axes of the coordinate system are defined as x and y, where x is measured along the top from the north end (away from the "exhaust end") of the case, and the circumferential y axis is measured with respect to its origin at the x axis, which runs along the top of the cylindrical shell. The north end of the case is located at x = –50, and, therefore, the origin of the x axis is located 50 cm south from the north end. The circumferential direction has a positive sign for locations accessible from the west of the cylinder.

The data from the accelerometers were recorded using two types of instrumentation systems. For the preliminary effort at Aerospace on a segment of an empty booster case, a Tektronix digitizing oscilloscope, model TDS 540A, was used to digitize data at a rate of 250 kHz. Later data and data taken at Edwards AFB on the inert-filled booster were recorded using a Hitachi 166 MHz laptop with a National Instruments digitizing, PCMCIA card, model DAT-1200. For the impact tests to the inert-filled booster, AC power was used to power the instruments. For the road tests, however, a 12-V car battery with a DC-to-AC power converter was used to power the system. The Tektronix oscilloscope had only 4 channels, whereas the laptop based system had 8 channels. Data from the oscilloscope required conversion from binary to ASCI format prior to data analysis. Data were analyzed using IGOR software available from Wavemetrics.

The accelerometers used in the sensors were the model 250, ±50 g from Analog Devices. In retrospect, the 5-g sensors should have been used for increased sensitivity. For tap testing performed with

25

the empty booster at Aerospace, these were adequate. However, for tests at AFRL, they were inadequate due to the low response and the high damping experienced with the inert booster. The 3 dB response bandwidth (single pole) is 1.2 kHz. The booster shell was tapped using either a hard plastic impact hammer, a rubber mallet, or a wooden stick.

A switching filter was used to provide low-pass filtering as an anti-aliasing filter. An 8th-order elliptic, switched-capacitor filter (MAX7400CPA from Maxim) was selected. The signal-to-noise ratios for these filters are quite good, better than –60 dB over a 0.5 to 5.0 V input. However, below 0.1 V, the signal-to-noise ratio drops precipitously due to clock-noise leakage. Performance will be poor if signal levels are low or if signals vary over a high dynamic range. Signals for the impact test and road tests were generally near 1 g or less (38 mV for a $\pm$50 g accelerometer) and are sufficiently low that the signal-to-noise ratio would be poor. Use of a more sensitive accelerometer such as the ADL 105, a $\pm$5-g full-scale accelerometer would provide more than adequate signals for peak acceleration events.

For generating the wave-induced acceleration data, a rubber hammer with a sensor was used to impact the motor surface at predetermined locations along the line (longitudinal or circumferential) on which the accelerometers were mounted for each set of accelerometer arrangements. The rubber head of the hammer is approximately 4 in. long by 2.5 in. in diameter. The objective was to record the wave arrival time at each accelerometer from each impact. The impact locations for the longitudinal wave speed calculations were (–45, 0), (5, 0), (55, 0), and (105, 0). The impact locations for the circumferential wave speed calculations were (50, 0), (50 35), (50, –50), and (50, –100).

4.3   Data Analysis

The wave speeds were measured in the two principal directions, the longitudinal and circumferential. The wave speeds in any other direction can be determined using Eq. (1). It should be noted that the phase of the wave may vary in directions between the two principal directions, as observed by Olofsson.[1] The motor case is a shell composite structure, and there are two types of associated speeds. One is associated with the fiber material modulus and its density. For example, the longitudinal wave speed V_L of graphite fibers is $(E/\rho)^{1/2}$. This longitudinal wave speed associated with Young's modulus of the graphite fiber is very high, over 10 km/s. This wave can be observed as a disturbance arriving promptly, and no transit time information can be obtained. This wave was observed only when the edge of the cylindrical shell was tapped. The other type of wave is the structure response-induced wave whose frequency depends on the structural design and boundary conditions. The waves associated with the structural/elliptical deformation response of the tube were recorded when excited by taps normal to the exterior cylinder surface of the composite shells, and the resulting waveforms were used to determine their speeds.

Since the solid rocket motor case material, made of graphite/epoxy composite using a filament winding technique with a symmetric lay-up, has macroscopic orthotropic material properties, the wave speed for the composite is directionally dependent. Because of the orthotropy, it is expected that the deformation wave speed on the longitudinal-circumferential plane will take an elliptic form, i.e.,

$$V^2(\theta) = [V_x\cos(\theta)]^2 + [V_y\sin(\theta)]^2, \tag{1}$$

where θ is the angle between the longitudinal direction and the direction of interest. This equation is a phenomenological description of the propagating wavefront. It is also applicable to a propagating deformation wave in a flat plate. For isotropic[2,3] and orthotropic plates,[4] the Kirchhoff plate equations were shown to be a good model for the deformations. Kirchhoff models, in general, are precise solutions to the deformation of the surface as a function of time. They show that the wave speeds exhibit dispersion effects, whereby the wave speeds are a function of frequency. Yet, we may reconcile this difference between Eq (1), which assumes constant speed, and the Kirchhoff equations by restricting the wave speed to a narrow frequency regime whereby the speed is constant. Along the circumferential and longitudinal directions of a composite tube, the position of the wave was shown to be linear with time.[1] Agreement of the data with the modeling results for a cylindrical tube using a finite-element code was good in the circumferential direction for position and speed. In the longitudinal direction, agreement was good for the speed and fair for position, but, in all cases, position was linear with time. Simple plate models for the wavefront such as Eq (1) appear to be applicable to tubes. Hence, measured speeds on the rocket motor could be related to the waveforms observed by accelerometers and strain gauges. Accelerometer data could be analyzed for its frequency content, and a distance could be calculated based on the dispersion characteristics of the traveling waves that constitute the tube dynamics. Eq (1) was adopted under the assumption of elliptical waves for a plate and the decomposition of velocity for the two principle directions.

When the recorded wave data were analyzed, it was found that the wave arrival time, based on the visual inspection criteria of peak amplitude, did not provide consistent values. Upon a careful evaluation, it was determined that the impact generated a wide range of frequencies whose speeds varied considerably. Because of this, the calculated apparemt wave speed depended on the location that was impacted and on the object used to tap the empty shell. When the accelerometer was located at a distance greater than 100 cm from the impact, much of the high-frequency component of the waves was attenuated, and, therefore, the recorded wave arrival times at different accelerometers did not correspond to the same frequency or the same frequency range. The calculated wave speeds varied by as much as a factor of 2 from one dataset to another.

Assuming that the source of the discrepancy was due to dispersion or frequency dependent speeds, it was decided to choose a specific frequency range common to all the datasets. The filtering procedure is important in eliminating the high-frequency components, which have higher speeds, as shown in solutions to the Kirchoff equation. These high frequencies are only present for sensors close to the impact site since the high frequencies are attenuated rapidly with distance. Fourier spectrum analyses to produce power spectrum densities (PSD) were performed for all the waves. A frequency range between 500 and 1000 Hz was selected. The wave-time history within the selected frequency band was analyzed by first performing a Fourier transform, eliminating the contribution outside the frequency band, and then performing an inverse Fourier transform. This filtering procedure gave a longitudinal wave speed of 268 m/s with a standard deviation of 38 m/s, and a circumferential wave speed of 419 m/s with a standard deviation of 31 m/s. Figures 4-1 and 4-2 show typical linear fits of distance vs. arrival times for the filtered waves. Speeds were also measured by Olofsson[1] who used a laser holography method on small graphite tubes. He observed speeds of 400 and 500 m/s in the longitudinal and circumferential directions, respectively.

Impact data using a calibrated impactor with a 5/8-in. tup and a 30-lb proof mass produced impact histories with frequency content below 200 Hz but little above 200 Hz. Hence, the speeds measured

and reported just previously are not valid for location of impacts by the calibrated impactor using the 5/8-in. tup on a 30-lb proof mass. For this reason, this mass was subsequently changed to a 10-lb proof mass for the tests performed at Edwards on the inert-filled booster to increase the frequency content of the vibrational waveforms.

Additional data was taken using the rubber hammer described earlier as an impact source. This data has lower frequency content than the dataset taken just prior to the impactor data, which used a plastic tipped hammer. Speeds from this dataset have not yet been analyzed. For this study, sensors and their locations were as shown in Table 4-1.

The impact locations for the rubber mallet were (185,0), (130,0), (80,0), (230,0), (50,80), (90,70), (180,70), (180,105), (180,35), (130,35), (130,70), (130,105), (130,–50), (80,–50), (80,–105), (80,70), (80,105), (–10,50), (–10,105), and (–10,–50). The data sample rate was 2 kHz with 12 bits of precision using the laptop-based data acquisition system. The data must be Fourier filtered into the appropriate frequency band from which the speeds may be derived. Data from impacts at these locations should be adequate to derive speeds throughout the entire empty booster shell. A preliminary analysis showed curvature in the speed when the unfiltered data are used.
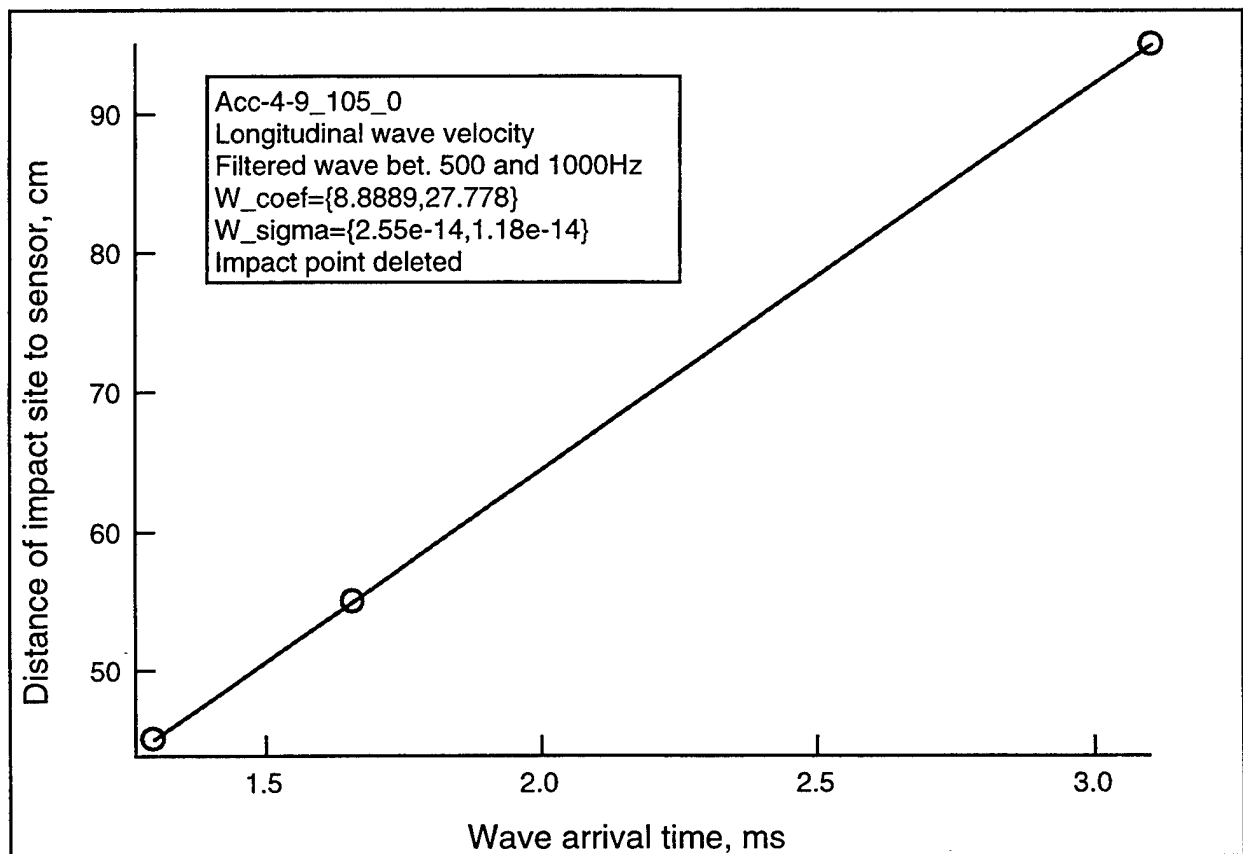
Figure 4-1. Typical arrival times of impact at sensors in the longitudinal direction for a single impact point at (105, 0).

28
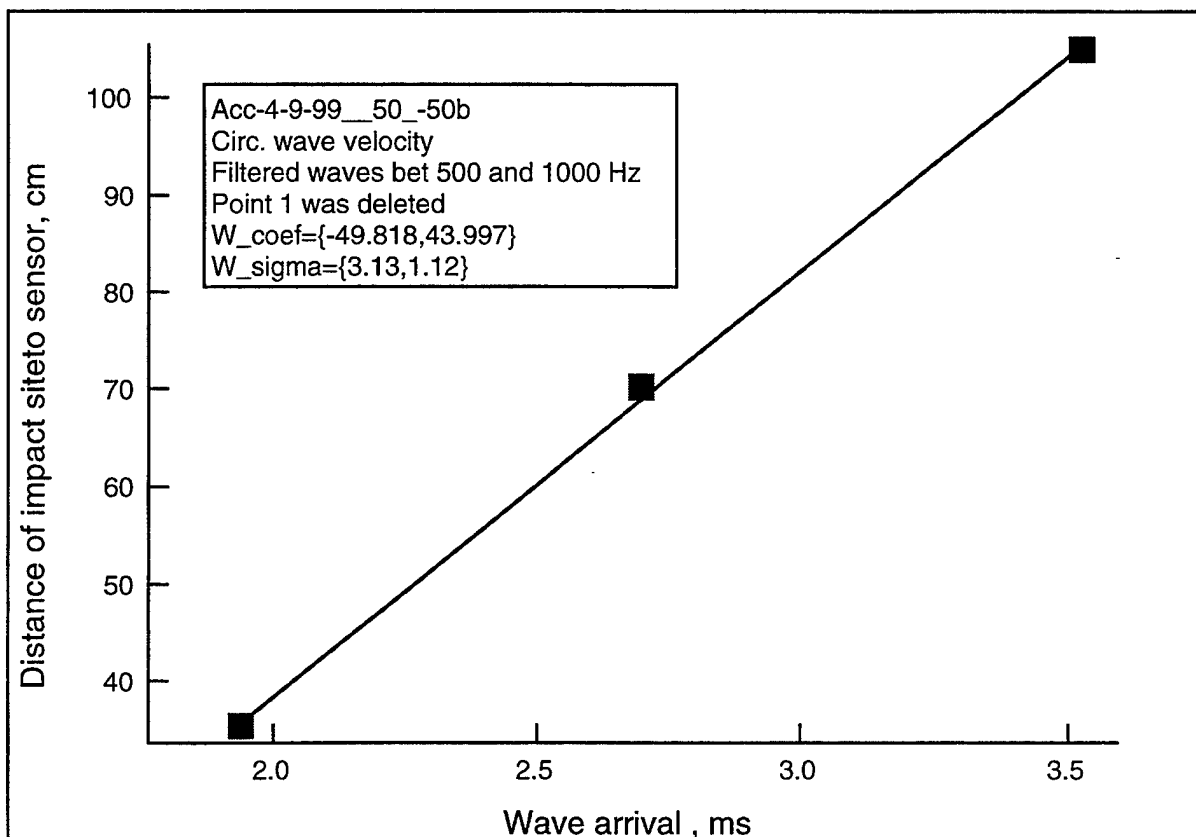
Figure4- 2. Typical arrival times of impact at sensors in the circumferential direction for a single impact point at (50,-50).

Table 4-1. Sensor Locations for Impacts with Rubber Hammer

Sensor ID	Sensor-Channel number	Location*(longitudinal) (cm)	Location* (from top, circumferential) (cm)
1	2 axis, longitude	0	0
2	2 axis, circumferential	0	0
3	2 axis longitude	200	0
4	2 axis, circumferential	200	0
5	1 axis longitude	175	-70
6	1 axis longitude	50	70
7	1 axis longitude	130	40
	Rubber mallet	various	various

*The coordinate system is the same as defined in section 2.

For the solid rocket motor case filled with an inert propellant, the situation was different. The inert propellant is a highly viscoelastic material. The material has many ingredients, including HTPB, NaCl (20 to 200 μm size particles), and aluminum particles (200 mesh). They generate high internal friction during deformation and thus have very high damping. The waves damped very rapidly at only a short distance away from the impact point. Therefore, the 50-g accelerometers were not suffi-

ciently sensitive to generate useful information. Separate measurements with more sensitive acceler-
ometers would be needed.

Since the inert-propellant-filled motor case would have a significantly different structural frequency
response from the unfilled case, the wave speeds for the two motor cases would be different. The
establishment of the wave speed for the filled case is necessary. The technique would be similar to
what was described for the unfilled case.

4.4   Triangulation for Impact Location

The determination of the impact location during the monitoring of a solid rocket motor case has much
utility. This approach should be applicable to all types of sensing devices, such as strain gages,
accelerometers, and fiber optics. This section describes the mathematical derivation necessary to
determine the impact location using the wave arrival time of three sensors at three distinct locations.

Since the motor case is made of high-modulus graphite fibers with epoxy as a resin, its mechanical
properties are, in general, anisotropic. The symmetric fiber lay-up with respect to both longitudinal
and circumferential directions makes its elastic properties orthotropic in the two-dimensional sense
since the thickness of the composite is much less than either the longitudinal or circumferential
dimension.

The surface of the motor case is treated as a two-dimensional plane with longitudinal and circumfer-
ential directions as the principal directions. Let the longitudinal direction be designated as the X
direction, and the circumferential direction be designated as the Y direction in a rectangular coordi-
nate system. The origin (0,0) is arbitrary. In the derivation, the following symbols are used:

α: X coordinate of the impact location

β: Y coordinate of the impact location

X_1:   X coordinate of sensor No. 1

X_2:   X coordinate of sensor No. 2

X_3:   X coordinate of sensor No. 3

Y_1:   Y coordinate of sensor No. 1

Y_2:   Y coordinate of sensor No. 2

Y_3:   Y coordinate of sensor No. 3

t_1:   wave travel time to sensor location 1

t_2:   wave travel time to sensor location 2

t_3:   wave travel time to sensor location 3

V_x: Wave speed in X direction (known)

30

V_y: Wave speed in Y direction (known)

λ :   Ratio of V_y to V_x (V_y / V_x) (known)

The relation describing the contour of the wave front at time t_i is

$$\sqrt{[(X_i - \alpha)/V_x]^2 + [(Y_i - \beta)/V_y]^2} = t_i \quad i = 1,2,3 \tag{2}$$

The values of t_i are not known with regard to the time of impact, but the differences, $(t_2 - t_1)$ and $(t_3 - t_1)$, are measured for the purpose of locating the impact. Therefore, the three equations represented by Eq (2) can be rearranged to

$$\tag{3}$$

$$\sqrt{[(X_i - \alpha)]^2 + [(Y_i - \beta)/\lambda]^2} - \sqrt{[(X_1 - \alpha)]^2 + [(Y_1 - \beta)/\lambda]^2} = V_x(t_i - t_1) \quad i = 2,3$$

For convenience, let's designate

$$d_i = [(X_i - \alpha)]^2 + [(Y_i - \beta)/\lambda]^2, \qquad i = 1,2,3$$

The two equations represented by Eq (3) can be used to solve for two unknowns, α and β. Since these two equations are nonlinear, and a closed-form solution is not obvious, an iterative approach needs to be taken. We will estimate the initial values of (α, β) as (α_0, β_0).

Let's designate functions f_2 and f_3 to represent the expressions on the left-hand side of Eq (3) with the index i equal to 2 and 3, respectively. The Taylor's expansions of f_2 and f_3 in the vicinity of (α, β) gives,

$$f_i(\alpha + \Delta\alpha, \beta + \Delta\beta) = f_i(\alpha,\beta) + f_{i,\alpha}\Delta\alpha + f_{i,\beta}\Delta\beta, \tag{4}$$

where $f_{i,\alpha}$ and $f_{i,\beta}$ are partial derivaatives of f_i with respect to α and β, respectively, and $\Delta\alpha$ and $\Delta\beta$ are $(\alpha - \alpha_0)$ and $(\beta - \beta_0)$, respectively.

Explicitly, $f_{i,\alpha}$ and $f_{i,\beta}$ are written as follows:

$$f_{2,\alpha} = -(d_2)^{-1/2}(X_2 - \alpha) + (d_1)^{-1/2}(X_1 - \alpha) \tag{5}$$

$$f_{3,\alpha} = -(d_3)^{-1/2}(X_3 - \alpha) + (d_1)^{-1/2}(X_1 - \alpha)$$

$$f_{2,\beta} = [-(d_2)^{-1/2}(Y_2 - \beta) + (d_1)^{-1/2}(Y_1 - \beta)]/\lambda^2$$

$$f_{3,\beta} = [-(d_3)^{-1/2}(Y_3 - \beta) + (d_1)^{-1/2}(Y_1 - \beta)]/\lambda^2$$

31

A combination of Eqs (4) and (5) and the use of α_0 and β_0 leads to a linear matrix equation

$$\begin{bmatrix} f_{2,\alpha} & f_{2,\beta} \\ f_{3,\alpha} & f_{3,\beta} \end{bmatrix} \begin{pmatrix} \Delta\alpha_1 \\ \Delta\beta_1 \end{pmatrix} = -\begin{pmatrix} f_2(\alpha_0,\beta_0) \\ f_3(\alpha_0,\beta_0) \end{pmatrix} \tag{6}$$

This allows the determination of $\Delta\alpha_1$ and $\Delta\beta_1$, which are used to correct the initial estimate α_0 and β_0. After the correction, one replaces the respective values of α_0 and β_0 with:

$$\alpha_1 = \alpha_0 + \Delta\alpha_1$$
$$\beta_1 = \beta_0 + \Delta\beta_1 \tag{7}$$

The values of α_1 and β_1 are then used as the new values of α and β in an iterative process using Eqs (5), (6), and (7). The recurrence formula for the iterative process is expressed as

$$\alpha_i = \alpha_{i-1} + \Delta\alpha_i$$
$$\beta_i = \beta_{i-1} + \Delta\beta_i \tag{8}$$

The iteration continues until a convergence is reached with a specified convergence criterion.

The above-described procedure was coded into an Excel file, and some test cases were examined. In general, convergence is reached in five to six iterations when the input warrants a solution. Otherwise, divergence will occur. One example of convergence is shown in Figure 4-3. As can be seen, the convergence occurs in four iterations despite the starting estimate of the impact origin (0,0) being far away from the actual solution (50,0). A simple error analysis using 500-Hz filtered waveform data could be used to estimate the uncertainty in the triangulation. Assuming good signal-to-noise ratio, the effective bandwidth is 250 Hz due to the Nyquist criteria. Thus, for a 240 m/s speed, the uncertainty in position is about 1 m for the worst case. If we average over two measurements, the position uncertainty is about 0.7 m. This independent estimate is in reasonable agreement with the error in the converged solution of the iteration procedure.

For a system that has more than three sensors close to the potential impact location with good signal-to-noise ratios, various subsets of three-sensor groups can be taken to approximate corresponding impact locations. For example, if five sensors have recorded good signals, the $^5C_3 = 10$ three-sensor groups would give 10 possible estimates of impact locations.

A least-square fitting procedure can also be used to give the best estimate of the impact location. A least-square fit approach can be described as follows. Assume there are N (N>3) data (sensor) points.

Iterative procedure for approximate the impact origin								
Three sensors are used				Impact at (50,0)				

Wave velocity Vx =   24035 cm/sec

Wave velocity Vy=   34180 cm/sec

Velocity ratio lamda=   1.422092781

Sensor 1   x1=   -40 cm
          y1   0 cm

Sensor 2   x2   50 cm
          y2   70 cm

Sensor 3   x3   100 cm
          y3   -64 cm

trial values   alpha=   0
                 beta=   0

Measured data   t2-t1=   -1.70E-03
                  t3-t1=   -9.00E-04

alpha	beta	f1,1st term	f1,2nd term	f1,3rd term	f1	f2	delta alpha	delta beta
0	0.00E+00	70.16356866	-40	40.8595	71.023	91.292	45.590218	-14.3024
45.59022	-1.43E+01	59.44429247	-86.179082	40.8595	14.125	0.1185	4.0513025	15.82807
49.64152	1.53E+00	48.15170758	-89.64794	40.8595	-0.637	0.2409	-0.073543	-0.7907
49.56798	7.35E-01	48.70829771	-89.569468	40.8595	-0.002	-2E-04	-0.000526	-0.00161
49.56745	7.33E-01	48.70943571	-89.568936	40.8595	-4E-09	3E-09	1.875E-10	-6.5E-09
49.56745	7.33E-01	48.70943571	-89.568936	40.8595	0	0	0	0
49.56745	7.33E-01	48.70943571	-89.568936	40.8595	0	0	0	0
49.56745	7.33E-01	48.70943571	-89.568936	40.8595	0	0	0	0

Figure 4-3. Illustrative example for triangulating impact location using three sensors.

Define

$$\Delta_i = (\sqrt{d_i} - \sqrt{d_1}) - V_x(t_i - t_1) \qquad i = 2...N$$

$$\Delta^2 = \sum_{i=2}^{N} \Delta_i^2$$

Using the least-square approach with α and β as unknowns, one has

$$\Delta\frac{\partial\Delta}{\partial\alpha} = \sum_{i=2}^{N}[(\sqrt{d_i} - \sqrt{d_1}) - V_x(t_i - t_1)][\frac{(x_i - \alpha)}{\sqrt{d_i}} - \frac{(x_1 - \alpha)}{\sqrt{d_1}}] = 0$$

$$\Delta\frac{\partial\Delta}{\partial\beta} = \sum_{i=2}^{N}[(\sqrt{d_i} - \sqrt{d_1}) - V_x(t_i - t_1)][\frac{(y_i - \beta)}{\sqrt{d_i}} - \frac{(y_1 - \beta)}{\sqrt{d_1}}]/\lambda^2 = 0$$

or (8)

$$\sum_{i=2}^{N}(\sqrt{d_i} - \sqrt{d_1})[\frac{(x_i - \alpha)}{\sqrt{d_i}} - \frac{(x_1 - \alpha)}{\sqrt{d_1}}] = \sum_{i=2}^{N}V_x(t_i - t_1)[\frac{(x_i - \alpha)}{\sqrt{d_i}} - \frac{(x_1 - \alpha)}{\sqrt{d_1}}]$$

$$\sum_{i=2}^{N}(\sqrt{d_i} - \sqrt{d_1})[\frac{(y_i - \beta)}{\sqrt{d_i}} - \frac{(y_1 - \beta)}{\sqrt{d_1}}]/\lambda^2 = \sum_{i=2}^{N}V_x(t_i - t_1)[\frac{(y_i - \beta)}{\sqrt{d_i}} - \frac{(y_1 - \beta)}{\sqrt{d_1}}]/\lambda^2$$

The values of α and β can be solved iteratively in a way similar to that described for Eqs (4) through (7) in the three-sensor case. Conversely, a general two-dimensional fitting procedure may be used as implemented in the IGOR software package from Wavemetrics.

This least-squares approach was not tested due to time constraints, but is considered to be a sound approach. Prior to its consideration, a simpler, cruder test of the elliptical speed profile was considered. Unfiltered data was used to derive the longitudinal and circumferential speeds, and the expected arrival times at sensors were plotted against the measured arrival times, again unfiltered. In general a 1–2 ms error was observed, which translates into approximately a 0.8-m error. With a least-square fit, a more self-consistent speed, and well-defined arrival times at the sensors, the error in localization of the impact site is expected to improve significantly.

4.5   Road Tests of GPS Position Location

In addition to the accelerometer measurements, GPS position information was recorded during road tests with the inert motor. The instrumentation consisted of a GPS receiver with data logging software on a laptop. General information includes position as a function of time, the number of satellites seen by the receiver, velocity, etc. Since GPS time is very accurate, it is simple and convenient to synchronize observed events to it from the laptop display. Events were noted on a log book with regard to a wrist watch and the offset time was noted to the GPS clock time. The log book events could then be corrected for the offset.

Accuracy for civilian non-differential GPS is limited to 100 m. The GPS receiver was situated on the top of the driver cab of the GEM transport vehicle, the highest point of the combined tractor-flatbed-inert booster configuration. Location readings were logged at the rate of one per second. Observa-

34

tions of time of events and landmarks were made from a chase car and time-correlated to GPS position information.

The GPS data and the logged observations listed in Tables 4-2 through 4-4 can be used to correlate acceleration or strain events with particular locations or road hazards experienced via time correlations. Its use is discussed by Amimoto.[5]

The hangar that houses the GEM under study is located at 117° 41.07′ West longitude, 34° 55.89′ North latitude. A list of recorded data is shown in Table 4-2. Examples of road tests are shown in Tables 4-3 and 4-4. The corresponding track mapping for the 3-mile route related to Table 4-4 is shown in Figure 4-4.

Table 4-2. List of GPS Data Files Recorded During Road Tests

File	Start Time	End Time	Description
GPS1	14:06:16	14:06:49	Stationary at hangar
GPS2	14:07:06	14:17:22	Drive around hangar, 1 loop
GPS3	14:17:40	14:24:53	Drive around hangar, 2 loops
GPS4	14:25:07	14:34:10	Drive around hangar, 2 loops
GPS5	14:34:27	14:50:36	Small maneuvers at hangar
GPS6	14:50:38	15:09:54	Short drive on roads
GPS7	15:10:34	15:40:54	Three-mile drive to Propellant Storage Complex and back to hangar

Table 4-3. Observations and Position Information During Road Tests Drive on Roads (File GPS6)

Comment	Time	117 W Lon (min)	34 N Lat (min)
Short Drive on roads begins	14:51:20	41.07	55.90
Driveway from hangar	14:53:30*	41.32	55.90
Strap Breaks	14:54:30*	41.33	55.92
Part 2 of drive starts moving	15:02:51	41.30	55.91
Left turn from Mercury	15:04:51	41.46	55.82
Right turn	15:05:10	41.47	55.78
Right turn	15:05:31	41.53	55.74
Right turn onto Mercury from Mars	15:05:48	41.58	55.75
Right turn	15:06:25	41.45	55.86
Left turn	15:06:59	41.22	55.87
Right turn	15:07:06	41.19	55.89
Dirt road	15:07:23	41.12	55.90
Right turn	15:07:38	41.07	55.90
Stop, back at hangar	15:07:48	41.07	55.89

Table 4-4.   Three-mile drive from hangar to Propellant Storage Complex and back to hangar (File GPS7)

Comment	Time	117 W Lon (min)	34 N Lat (min)
Begin	15:13:51	41.07	55.88
Indus and Persea on Antares Road	15:15:25	41.18	55.87
Left turn	15:16:00*	41.46	55.83
Left onto Mars from Mercury, bump	15:16:56	41.59	55.74
Bump	15:18:06	41.38	55.44
Travelling at 20 mph	15:18:37	41.26	55.33
Continuing on straight road	15:21:07	40.61	54.76
Left turn	15:23:23	40.03	54.24
Right turn	15:23:43	39.99	54.26
Stop at Propellant Storage Complex	15:23:59	39.97	54.25
Back onto pavement	15:30:16	39.99	54.24
Travelling at 40 mph, straight road	15:31:01	39.98	54.22
Travelling at 35 mph, straight road	15:33:43	40.92	55.04
Road curves to right	15:34:53	41.39	55.47
Passed over 2 bumps	15:35:38	41.56	55.71
Right turn on Mercury from Mars	15:35:51	41.58	55.74
Right turn on Antares	15:36:27	41.44	55.87
Left on Indus	15:37:02	41.21	55.88
Right turn	15:37:09	41.18	55.89
On dirt at driveway to hangar	15:37:21	41.12	55.90
Stopped	15:37:45	41.09	55.90
Backing into hangar	15:38:36	41.10	55.92

*Estimated

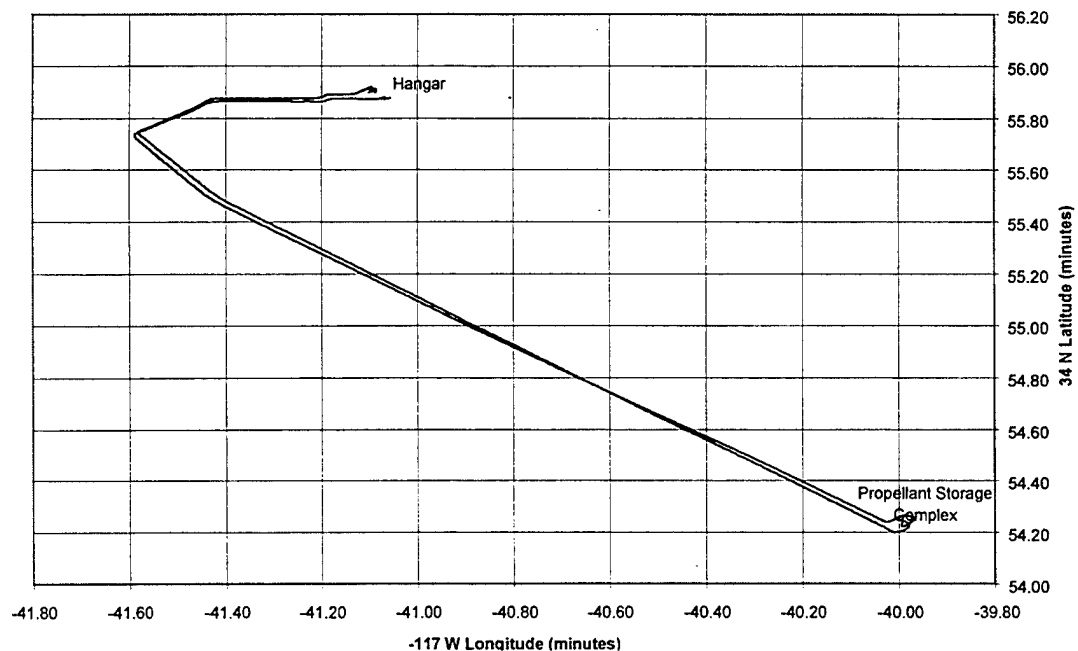Three Mile Drive to Propellant Storage Complex and Return to Hangar

Figure 4-4. Position track from File GPS7.

36

4.6   Lessons Learned

- Sufficient preparation time is needed to prepare instrumentation and test procedures. Dry runs are invaluable to meeting test schedules, and ensuring successful equipment operation and reliable data collection.

- Predicting the acceleration amplitudes is difficult for the field tests. It seems that sensitivities of 1–5 g are needed for the filled GEM, but the values should also be based on performance requirements of the components to be tested.

- Several test opportunities are needed not only to test out equipment but to also understand configuration and validate test procedures.

- Additional effort is needed to quantify the impact-induced wave speeds and how well localization of impact site can be achieved.

4.7   Conclusions

We have identified an approach to the measurement of wave speeds in composite solid rocket motor cases. Frequency filtering must be used on the observed waveforms to derive consistent values of wave speed to overcome the dispersion effects predicted by the Kirchoff equation. Some care must be taken to examine the frequency content of impacts in order to select an adequate frequency range for the speed measurement. For free-fall impacts, variations in the mass of the impacting object, the softness of its impacting face, and the stiffness of the object under impact will generate waves with various frequency ranges and thus will produce inconsistent wave speeds. These speeds can be used in an elliptical model with a least-square approach to localize the origin of the impact. These wave speeds are associated with structural deformations and not the prompt, longitudinal wave component associated with the modulus of the fiber. This work then validates the assumptions that enables one to find the impact location on the composite booster. More sensitive accelerometers, 1 to 5 g, must be used to overcome the damping that is observed when the inert propellant is present. Lastly, the use of GPS position recordings has high value to correlate position with acceleration or other events of note.

4.8   References

1. K. Olofsson, K. E. Fallstrom, and P. Palagyi, "Laser generated and recorded transient bending waves in composite tubes," 36, pp 224-231, 1996.

2. E. Fallstrom, H. Gustavsson, N. E. Molin, and A. Wahlin, "Transient Bending Waves in Plates Studies by Holographic Interferometry", *Experimental Mechanics*, 29 (4), pp 409-413, 1989.

3. K. E. Fallstrom, L. E. Lindgren, N. E. Molin, and A. Wahlin, *Experimental Mechanics*, 29 (4), pp 378-408, 1989.

4. S. Urgela, "Grading of wooden plates for musical instrument making by means of holographic interferometery," Opt. Eng., 37, pp 2108-2117, 1998.

5. S. T. Amimoto, R. Crespo, E. W. Fournier, M. A. Kwok, H. Ozisik, R. Y. Robinson, and E. M. Yohnsee, "Atlas Payload transporter vibration and acceleration characterization using MEMS sensors at Vandenberg AFB", Aerospace Report, no. TOR-98(8260)-1.

5. Acoustic Emission Testing of the Delta Graphite/Epoxy Rocket Motor (GEM) (J. P. Nokes)

5.1   Abstract

Acoustic emission (AE) monitoring was evaluated as a potential health monitoring technique for Delta graphite/epoxy motors (GEM). The results of this investigation showed that AE was sensitive to the higher frequency (>100 kHz) components of the stress wave generated by the impact. The lowest energy impacts (1 ft-lb) were easily detected at distances of 1 m, while higher energy impacts (6 ft-lb) were detected at distances more then 3 m from the impact source. Additional testing was conducted to evaluate the effect of typical lifting operations on the GEM. AE monitoring of these operations did not produce detectable acoustic indications, suggesting that the resulting loads were below the damage threshold.

All of the AE monitoring was done using a commercial six-channel system. The six sensors were arranged into a number of configurations to determine an approximate number of sensors that would be required for complete acoustic coverage of the GEM case. The results of this experimental investigation indicate that an array of ~10 sensors could provide full coverage for a GEM without cork insulation. This sensor array would have sensitivity to impacts on the order of 3–6 ft-lb.

These preliminary experiments indicate that an AE-based health monitoring system is within the capabilities of current AE technology. However, additional testing and technique development would be required to optimize an AE health monitoring system specifically for the GEM. This testing should include an evaluation of alternative acoustic transducers and monitoring equipment as well as specific acoustic characteristics of the GEM (cork insulation, skirt region).

5.2   Introduction

The failure of a (G)raphite/(E)poxy solid rocket (M)otor (GEM) during flight in early 1997 and the subsequent investigation precipitated an extensive investigation into potential failure modes for the composite case. One credible scenario proposed an undetected impact event occurring during GEM transportation or handling. The impact damage might significantly degrade the case strength and yet not be obvious to a cursory visual inspection. This possible damage scenario sparked a community-wide interest in mitigating the risk of an undetected impact event.

An investigation was undertaken at The Aerospace Corporation to evaluate different approaches to health monitoring of the GEMs. These approaches included resistive and optical strain gages, accelerometers tuned to different frequencies, impact sensitive paints, and acoustic emission (AE) monitoring. Each of these technologies has specific advantages and difficulties that were evaluated during this investigation. Of particular interest for this document is the application of AE techniques to the detection of stealth impact events: that is, impacts that could damage the case but would not leave a visible bruise on the case.

AE techniques are based on the detection and evaluation of internal fracture events that can occur within a structure that is placed under stress. These irreversible events produce vibrations that propagate through the structure as waves that can be used to monitor the initiation and growth of damage within the structure. This monitoring capability has been applied to composite structures that undergo proof testing (composite rocket motor cases and pressure vessels) to identify potential problems before the component enters its service life. AE has also been used for damage tolerance studies measuring the growth of delaminations in composites. In this case, the individual fracture events characteristic of delamination growth were isolated from the background AE. A map of the damage growth vs. applied load could then be generated from this data.

Current AE monitoring and evaluation systems utilize an array of piezoelectric sensors acoustically coupled to the structure's surface. The sensors are linked to a high-speed, computer-controlled data acquisition system. When a fracture event is detected, the AE system records the output from each sensor over a specific window of time. The complete set of sensor data provides insight into the wave propagation characteristics of the material. The AE data can be evaluated to extract the acoustic properties of the structure as well as the location of the fracture event by triangulation techniques.

Less complex AE systems are available that do not save the complete waveform, rather they record specific parameters related to the AE event. These parameter-based systems tend to have a faster acquisition rate than wave-based units and a lower cost. However, they are less reliable in determining event locations.

A simplified AE technique was used for the initial health monitoring study of the GEM. The goal was to determine the sensitivity of the AE transducers to low-energy impact events that were below the damage threshold of the composite material. In this investigation, AE was used as a sophisticated microphone to detect the case impact in real time. While this approach does not utilize the full capabilities of the wave-based AE system, it best meets the requirements for health monitoring of the GEM.

5.3 Equipment

The experimental testing at AFRL/EAFB was performed using a Digital Wave Corp. 6-channel AE system. The unit consists of external pre-amplifiers that allow as much as 40 dB of gain to the transducer output, a primary amplifier unit with an additional 45 dB of gain, frequency filtering, trigger gain, and threshold. The output from the main amplifier is used as input for the computer-controlled digital acquisition system. The AE system was used in conjunction with six Digital Wave model (B-1025) transducers. These small (15 mm X 8 mm) transducers weigh 4.5 g and have a flat frequency response between 100 kHz and 1 MHz. . The transducers were held to the case using Velcro bands looped around the motor. A water-based acoustic coupling gel (Sono-Trace) was used to enhance the acoustic coupling between the transducer and the case. The Velcro bands allowed for fast and convenient changes to the transducer array. In a fixed system, the transducers could be permanently mounted to the case. The transducers were connected to the preamplifiers with 6-ft lengths of cable. Again, in a production system in-line amplifiers could be used to eliminate the need for the external preamplifiers and the associated hardware.

5.4   Experimental Procedure

The impact experiments were performed at the AFRL/ EAFB Test facility. An inert Delta GEM was made available to Aerospace for a series of low-energy impact tests using a calibrated impactor. For these initial tests, two sensor configurations were used. The sensor placement and the relative impact position for each configuration is illustrated in Figure 5-1.

Configuration 1 was used to examine the effect of anisotropy in the composite case, while configuration 2 was designed to evaluate the sensor spacing required for detecting impact events over the length of the GEM.

The impacts were generated using a 0.625-in. steel tup mounted to a pendulum designed to impart a known impact load at specific drop heights. Three energies, 1, 3, and 6 ft-lb were examined during this experiment. These were all below the damage threshold for the GEM.

For each impact, the resultant AE activity in the GEM was recorded at a digitizing rate of 5 MHz. The resulting waveforms were stored to disk for future evaluation. In order to maximize the detectability of the low-energy impacts, both the signal and trigger gains were set to levels that would be inappropriate for traditional AE monitoring. Future experiments could optimize the gain setting for specific impact levels.

Additional experiments were performed to evaluate the loads on the GEM due to lifting operations. Several operations were performed where the GEM was pivoted about the chocks both forward and aft of the center of gravity. The AE sensors were arranged on the case in these areas and were monitored during the procedures.
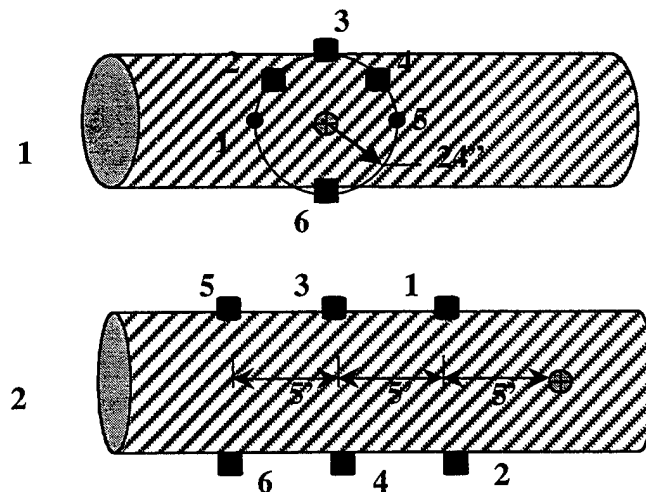

Figure 5-1. Sensor arrangements used for the GEM experiments.

5.5 Results

In these preliminary tests, the primary goal was to detect the occurrence of the impact events. The instrument gains were set to relatively high values (76 dB) to ensure that the low-energy impacts were detected. The high gains led to saturation in the recorded waveforms for the 3 and 6 ft-lb impacts. Typical examples of the event data for the three different impact energies are shown in Figures 5-2 through 5-4. These are the waveforms recorded at sensor 3 located 2 ft from the impact site. In each case, AE activity related to the impact event arrived at the sensor ~300 μs after the impact. However, in the 3 ft-lb and 6 ft-lb case, the AE signal contains additional components that are completely saturated beyond this point. While the amplitude data was corrupted by the signal distortion, the arrival times were not.
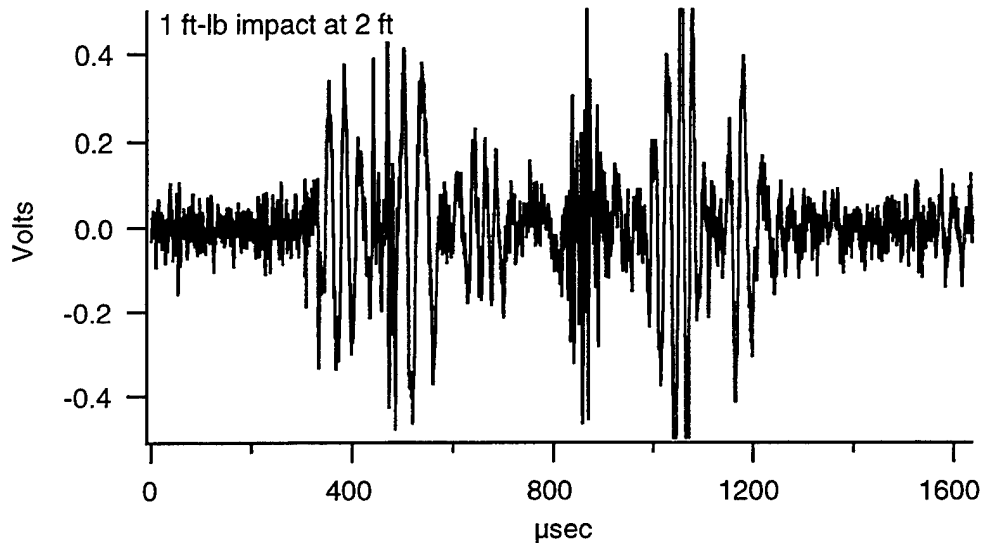

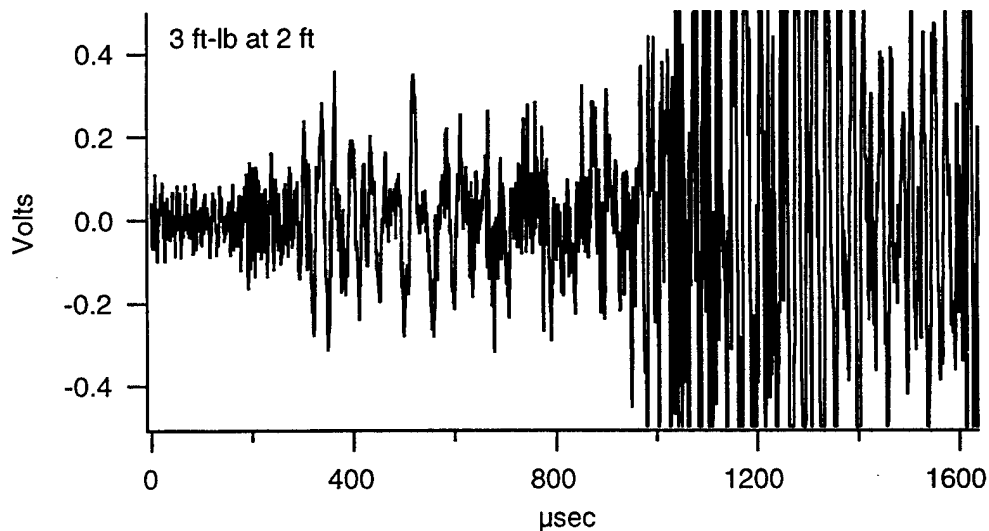Figure 5-2. AE signal of a 1-ft-lb impact 2 ft from the sensor.

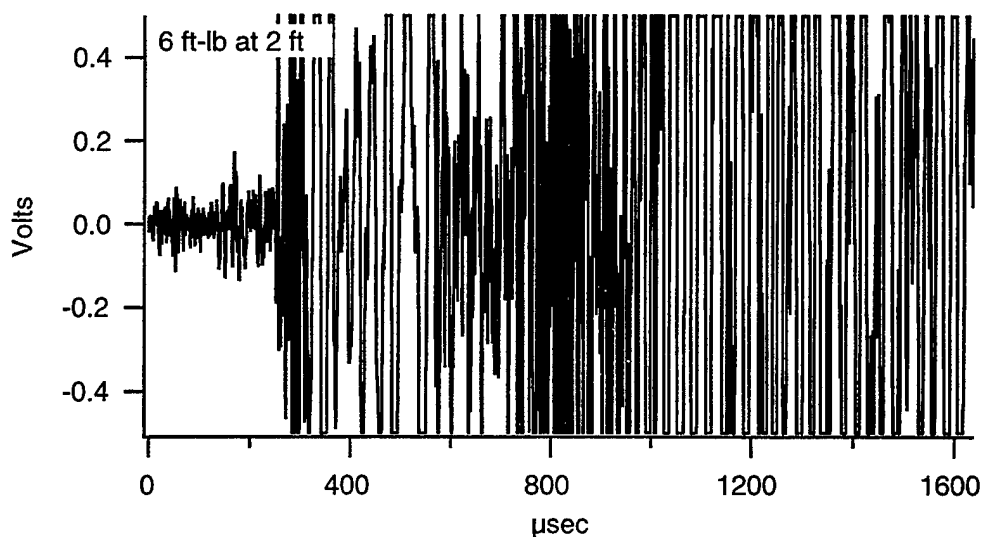Figure 5-3. AE signal of a 3-ft-lb impact 2 ft from the sensor.

42

Figure 5-4. AE signal of a 6-ft-lb impact 2 ft from the sensor.

Evaluation of the signals from the recorded data provided the approximate sensor spacing required to reliably detect impacts of various levels. as indicated in Table 5-1.

Table 5-1. Sensor Spacing Required to
Detect Low-Level Impacts

Impact Level (ft-lb)	Sensor spacing (ft)
1	4
3	10
6	>10

Additional testing was performed to evaluate the AE that is generated during handling operations. A number of lifts were done with the AE sensors located in the expected regions of high load. No events were detected.

5.6   Conclusions/Future Work

The preliminary data acquired during this experiment clearly indicates that low-level impact events can be reliably detected using AE sensors. Even for modest impact energies (<6 ft-lb), only a handful of sensors are needed to provide full coverage for the GEM. However, in order to implement an AE-sensor-based health-monitoring system, several additional studies must be completed, some directly related to AE monitoring of the GEM system and others concerned with the appropriate damage thresholds. These include:

- Evaluation of a parameter-based AE system. These instruments are less expensive then wave-based systems and may provide the necessary impact detection.

43

- Further evaluation of sensor placement and bonding techniques. It might be beneficial to bond the sensors directly to the case. This will avoid the use of coupling gels, but may impact transducer sensitivity.

- The effect of the external cork insulation on the measurement must be quantified. Delta GEM cases have external cork insulation to alleviate aeroheating problems. Unfortunately, the cork dramatically attenuates AE, limiting the sensitivity.

- Examine the use of PVDF film transducers as a replacement for the traditional crystal-based sensors. These low-profile transducer elements could eliminate the interference concerns of the mounted sensors.

- Repeat these experiments to verify the results and to add additional tests designed to utilize the benefits of wave-based AE.

Based on these preliminary experiments, an AE-based health-monitoring system is well within the capabilities of current technology. The key issue then becomes defining a pre-damage threshold acceptable to the aerospace community that accounts for different potential sources of impact (screw-driver, forklift) and calibrating the health monitoring system to screen for those events.

6. Full-Scale DELTA GEM MPS Demonstration
(J. V. Osborn, B. C. Brown, S. T. Amimoto, E. W. Fournier)

6.1 Introduction

Solid rocket Graphite/Epoxy Motor (GEM) casings are susceptible to catastrophic damage due to blunt force impacts.[1] Following the explosion of Delta 241 (IIR-1) on January 17, 1997, the failure investigation board concluded that the GEM casings should be inspected for damage just prior to launch. Subsequent investigations and feedback from industry has led to our proposal to instrument the entire fleet of GEMs from acceptance testing through erection on the launch pad with a continuous health monitoring system. This system would potentially monitor and record adverse impacts, accelerations, strains, or environments that may cause damage to the GEM casings.

The key requirements for such surveillance of GEMs are an unobtrusive system that does not interfere with normal rocket motor operations, direct-wire and wireless flexibility, very long-term surveillance capability in stand-alone wireless mode, low power, and the ability to distinguish normal operational signatures from unusual serious events. Interest by the Medium Launch Vehicle (MLV) Program Office in the potential long-term application of such a system prompted this demonstration on a full-scale inert Delta GEM rocket motor as described in this report.

Technology developed under the Microelectromechanical (MEMS) Systems Corporate Research Initiative, Multiparameter Sensor (MPS) task was applied in the present demonstration.[2,3,4] This multi-year research program has led, in this case, to the creation of a system concept that would allow the unobtrusive, continuous health monitoring of GEM casings and other impact-sensitive graphite/epoxy structures. Our system concept uses a combination of MEMS sensors organized with a wireless network such that both impacts and environmental information can be collected, stored, and forwarded to a central computer via wireless rf communication.

The purpose of this laboratory demonstration was twofold: first, to determine whether 3-axis accelerations measured at a single location could detect impacts along the body of a full-scale, loaded, graphite/epoxy composite motor; and second, to demonstrate that this sensor could be implemented with a wireless networked MEMS multiparameter environmental monitor measuring 3-axis acceleration, temperature, pressure, and humidity. This report describes the multi-parameter sensor suite and presents the results collected with the GEM MPS Health Monitoring System during a demonstration conducted at the Air Force Research Laboratory (AFRL) at Edwards Air Force Base (EAFB).

6.2 MEMS Wireless Multiparameter Sensor System

A MEMS Wireless Multiparameter Sensor is a combination of multiple microelectromechanical sensors measuring different environmental parameters integrated together with local computing, data storage, wireless communication, and power. The MPS is organized in a network such that hundreds of such nodes may communicate to a centralized data archiving computer (Figure 6-1). The need for

45

such a sensor network is not limited to GEM health monitoring. The MPS system may be employed wherever high-value assets are stored, transported, or handled, and where the history of shock, acceleration, temperature, humidity, or pressure is of concern to the operation or reliability of that high-value asset.

The present implementation of the MPS electronic hardware leverages off of commercially available technology to provide sensor data acquisition and processing, local memory storage, and networked rf communications. The design of the MPS is partitioned into an MPS sensor box and an MPS processor unit as shown in Figure 6-2. The partitioned design allows for customized arrangements of sensors to be tailored to a specific measurement, as well as to provide a common data collection, processing, storage, and communication infrastructure.

The primary goal of the MPS aspect of this demonstration was the development of a networked, wireless, MPS demonstration system capable of collecting and processing 3-axis acceleration, temperature, humidity, and pressure data from a MEMS sensor suite attached to the full-scale inert Delta GEM casing. This system can be scaled up such that up to fifty local-area MPS sensor collection sites can forward their data using a wireless network to a local data collection hub for data archiving or user display. Multiple local areas may be combined with a wired network such that hundreds to thousands of sensor nodes can be monitored over a large geographic area.

6.2.1   MPS MEMS Sensor Suite

In this demonstration a 2 x 2 x 4 in. metal box, shown in Figure 6-3, housed the MPS environmental sensors in addition to a 3-axis accelerometer sensor. The environmental sensing package consisted of the Ohmic HC-700 humidity sensor, the Motorola MPX5100A pressure sensor, and the Analog Devices AD592 temperature sensor. The environments sensor package was rigidly fastened to the interior top of the sensor box, and holes were drilled to provide the sensors with exposure to the ambient environment.
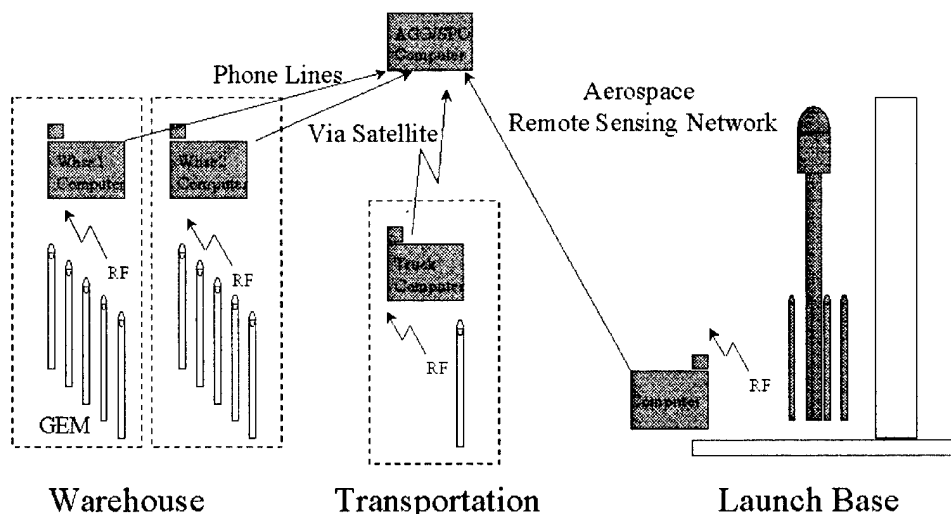

Figure 6-1.   MPS communication network concept showing coverage of high-value assets through storage, transportation, and pre-launch operations.
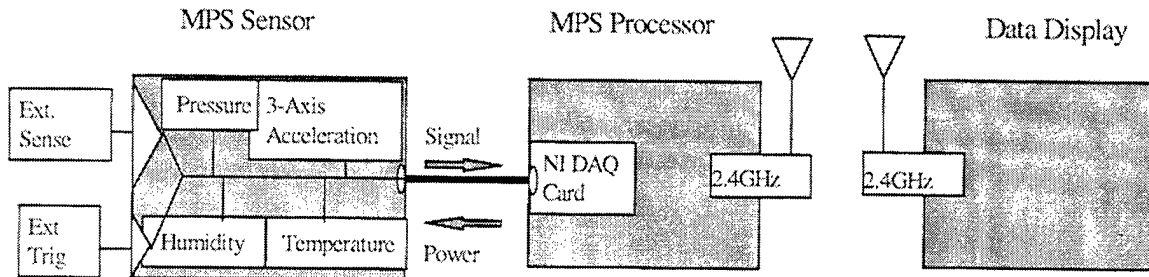
46

Figure 6-2. MPS signal acquisition and remote display block diagram showing the flow of information from the sensor front-end through the MPS data processor and wireless network to the remote user data display terminal. Fifty MPS nodes can be supported in one local area; multiple areas can be covered.
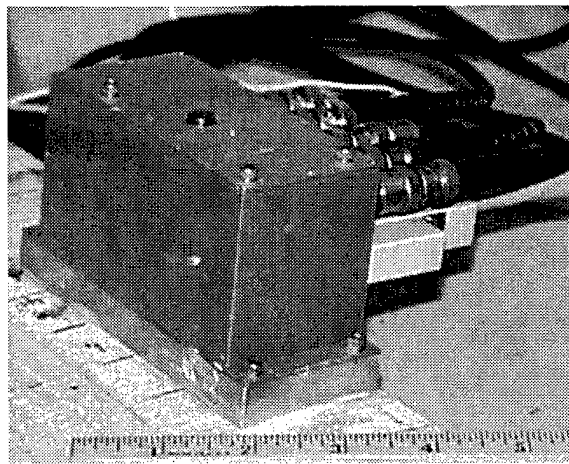

Figure 6-3. Multiparameter Sensor Package with 3-axis acceleration, temperature, pressure, and humidity sensors with optional interface to external sensors via BNC connections.

The dynamic sensing package housed within the same sensor box was a 3-axis accelerometer system consisting of one single-axis Analog Devices ADXL150 and one dual-axis ADXL250 accelerometer. To accurately capture the dynamic response of the test structure, it was necessary to decouple the acceleration response of the test structure from the acceleration response of the sensing package. System requirements, in general, prevent the accelerometers from being mounted directly to the test article. The solution, in this case, was to provide a rigid path with known material characteristics between the sensors and the test article. The vibrational conduit connecting the sensor packaging to the test structure consists of a solid aluminum MPS sensor mount and an aluminum accelerometer mounting block (Figure 6-4).

When assembled, the sensors are attached to adjacent sides of the accelerometer mounting block using a thin layer of epoxy. The mounting block was then rigidly fastened to the MPS sensor mount by two cap screws. The current GEM demonstrator incorporated a thin layer of epoxy as the fastener
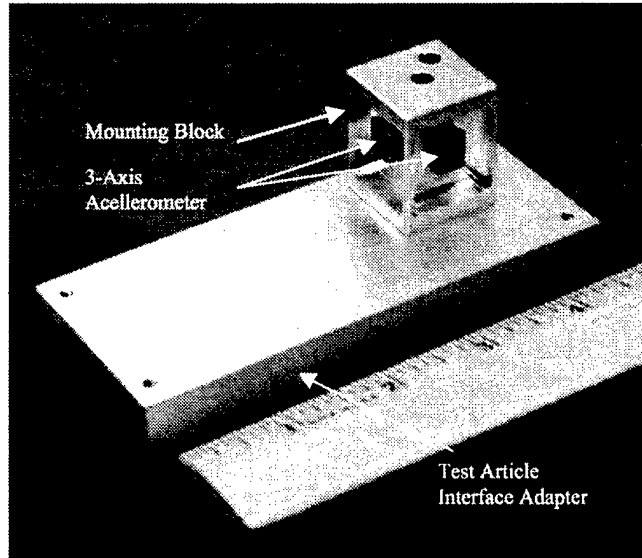
47

Figure 6-4. MPS sensor mounting adapter showing one single-axis MEMS accelerometer, one two-axis MEMS accelerometer, mounting block, and package interface to the GEM test article.
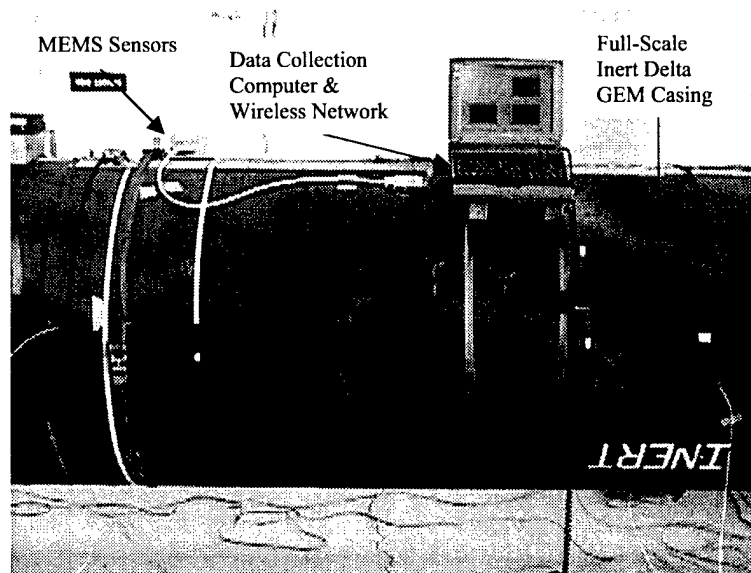

Figure 6-5. MPS sensor with data collection computer attached to Delta GEM during impact experiment testing. Data is collected at high speed, then forwarded wirelessly to a remote user display terminal.

connecting the MPS sensor mount to the GEM test article. Shown in Figure 6-5 is the COTS implementation of the MPS system with the sensor attached to the GEM casing and the wireless laptop collecting information from the test article. For these tests, the GEM test article was oriented horizontally on chocks, with the inboard surface pointing upward. The MPS was mounted on the top surface of the GEM case at the center-of-mass location. Coordinates, centered on the MPS, were chosen such that +X was parallel to the GEM axis from tail to nose, +Y was tangent to the surface of the case

from right to left when seen from the tail of the booster, and +Z was normal to the surface at the MPS location.

In addition to the environmental and dynamic sensing packages, the complete sensor assembly contained five mini-BNC connectors that served as optional input ports for trigger and external sensor inputs. Although unused in this demonstration, these inputs may be used to support customized sensors for a particular application. The combined signals were channeled through a National Instruments 68-pin shielded cable to the MPS data acquisition laptop computer. Power for the MPS sensors was provided by the laptop computer.

6.2.2   MPS Data Acquisition Computer

To reduce cost and effectively perform the GEM MPS demonstration with the most flexibility, we chose to implement the MPS data acquisition portion of the effort with a conventional COTS laptop computer and wireless local area network (LAN). As part of the MEMS CRI effort, we are developing custom palm-sized MPS hardware (Figure 6-6). This future version of the MPS will have 3-axis acceleration, temperature, pressure, and humidity sensors, a micro-controller, event storage memory, time keeping, wireless communication, and power, integrated into one miniaturized package.

A Hitachi VisionBook Plus 5000 with a National Instruments E-Series Data Acquisition Card processed the incoming analog sensor signals. The data sampling function of the MPS is provided by a commercially available 16-channel National Instruments DAQ PCMCIA card (AI-16XE-50) having 16-bit resolution. This card was configured for 3 high-speed channels, sampled at 25 ksamples/s, for accelerometer data collection, while three additional channels were used at a 500-Hz collection rate for non-time-sensitive environmental measurements (temperature, pressure, humidity). The software running the overall data acquisition process was developed in-house and based upon National Instruments LabView 5.0.
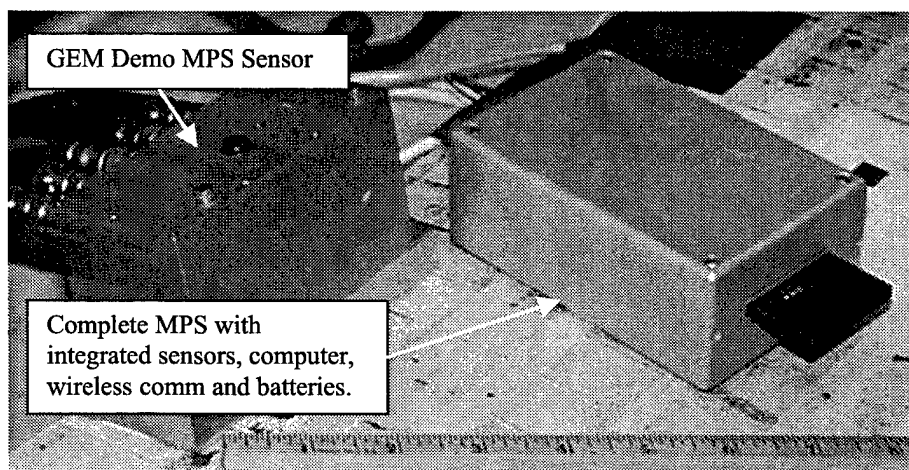

Figure 6-6.   GEM MPS demo sensor (laptop computer not shown) and future palm-sized design of the complete multiparameter sensor.

49

6.2.3 MPS Remote Data Display Computer

An important part of the demonstration was the wireless data exchange. A second Hitachi Laptop using a wireless LAN served as the display computer. The hard drives of the two computer were cross linked via the wireless network, with both having shared file access. The remote computer also used LabView software to access files and plot MPS data. The MPS user screen displayed the three-axis accelerations, pressure, temperature, and humidity measurements. As each new information packet was stored on the remote display hard drive, the graphs of the MPS display were updated (Figure 6-7).

6.3 Results

The MPS system was used in this demonstration to detect impacts, record impact impulse temporal waveforms, monitor the ambient environmental conditions and transmit these results wirelessly to a remote user terminal for data display and storage. The following section summarizes results related to these activities.

6.3.1 GEM Impact Testing

MPS impact acceleration data was collected with a 3-axis accelerometer located at the center of mass of the GEM casing. Accelerations were sensed with the Analog Devices Inc. ADXL-150 single-axis
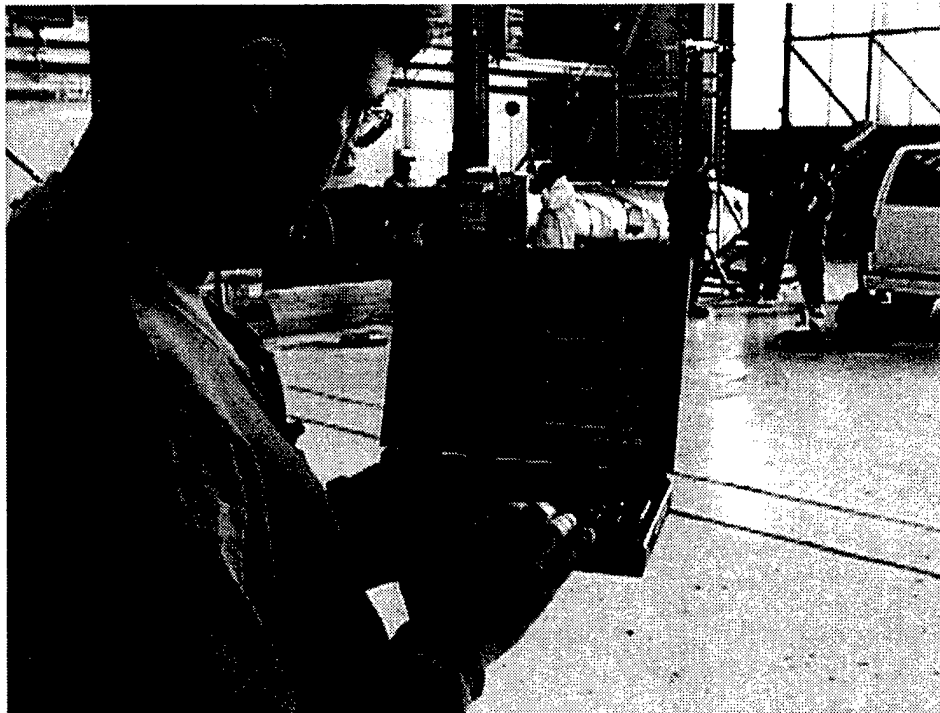

Figure 6-7. Remote user MPS display showing time sampled and Power Spectral Density (PSD) plots of accelerations for X, Y, and Z axes. Shown in background is the GEM test article with the wireless MPS sensor package mounted mid-ship.

50

and ADXL-250 dual-axis ±50-G accelerometers. Accelerometer system noise for each of the three axes was measured to be 64 mG, 62 mG, and 69 mG for the X, Y, and Z accelerometers, respectively. Frequency response of the accelerometers are specified to have a –3dB roll-off at 5 kHz.

Calibrated impact energies of 1 ft-lb, 3 ft-lb, and 6 ft-lb were created by impacting the side of the GEM casing with a fixed mass swung from various heights. The impact geometry was determined by the design of the impactor, which required that the impact mass be moving horizontally at the point of impact. As a result, the impact locations were always at points on the case with a surface normal that was parallel to the ground. The impact points were thus always offset by 90° from the location of the MPS. MPS data acquisition was triggered on the leading edge of the impact acceleration wave as it propagated along the GEM casing. The MPS system was configured to store 1000 points of the incoming wave at 25,000 samples per second.

Data for the 1, 3 and 6 ft-lb impacts for various positions away from the MPS are shown in Figure 8. In each plot the absolute value of the peak detected acceleration is plotted verses the axial component of distance away from the MPS sensor for each axis. Additionally, the root-sum-of-squares total peak acceleration is plotted. Data collected for impacts fore and aft of the MPS as well as data collected for impacts on the right side and left side are combined here and plotted as impacts at an absolute distance from the MPS. Right-side or left-side peak MPS impact responses are identical in magnitude due to the circular symmetry of the booster except for the phase of the impact wave. Fore/aft impact responses may in fact be slightly different due to an asymmetry along the booster from the thick-walled nozzle end to the thin-walled nose-cone end. Our MPS measurements did not detect this asymmetry as we were measuring impact-induced body accelerations that are only slightly affected by this fore/aft asymmetry.

Data shown in Figure 6-8 show that for impacts along the sides of the GEM casing, the majority of the accelerometer response was along the y-axis, across the GEM casing axial direction (i.e., along the direction of the impact). Accelerometer responses clearly dampen rapidly as the location of the impact is moved away from the MPS sensor. All impact energies were sensed when closer than 3.5 ft, while a 6-ft-lb impact transient wave could be sensed at a maximum distance of 10 ft. The maximum distance at which an impact could be detected was ultimately limited by the noise floor of the MPS sensor. Once the impact signal had decayed to less than twice the system noise (~100 milliGrms typ.) the impact could not be detected.

From this data, one can conclude that to develop a low-cost, minimal, distributed accelerometer network capable of detecting an impact with an energy equal to or greater than 6 ft-lb anywhere along the GEM, would require, as a minimum, a string of four single-axis accelerometers. These sensors would be located along the axis of the GEM, placed every 10 ft. This could be accomplished by simply distributing along the body of the casing, in a single string, the existing three MPS accelerometers, and using an additional internal MPS accelerometer. This spacing would cover a 40-ft-long casing (or potentially more) allowing for detection of any side impact with an energy greater than or equal to the 6-ft-lb damage threshold, anywhere along the GEM. The main shortcoming of this approach is that nearby impacts smaller than 6 ft-lb may also trigger the system, creating false impact alerts. This shortcoming would only alert operators to small impacts that were falsely identified as damaging; true damaging events would still be recorded as well. Due to the simplicity and ease of implementation, this limitation may be considered acceptable. An alternative approach would be to
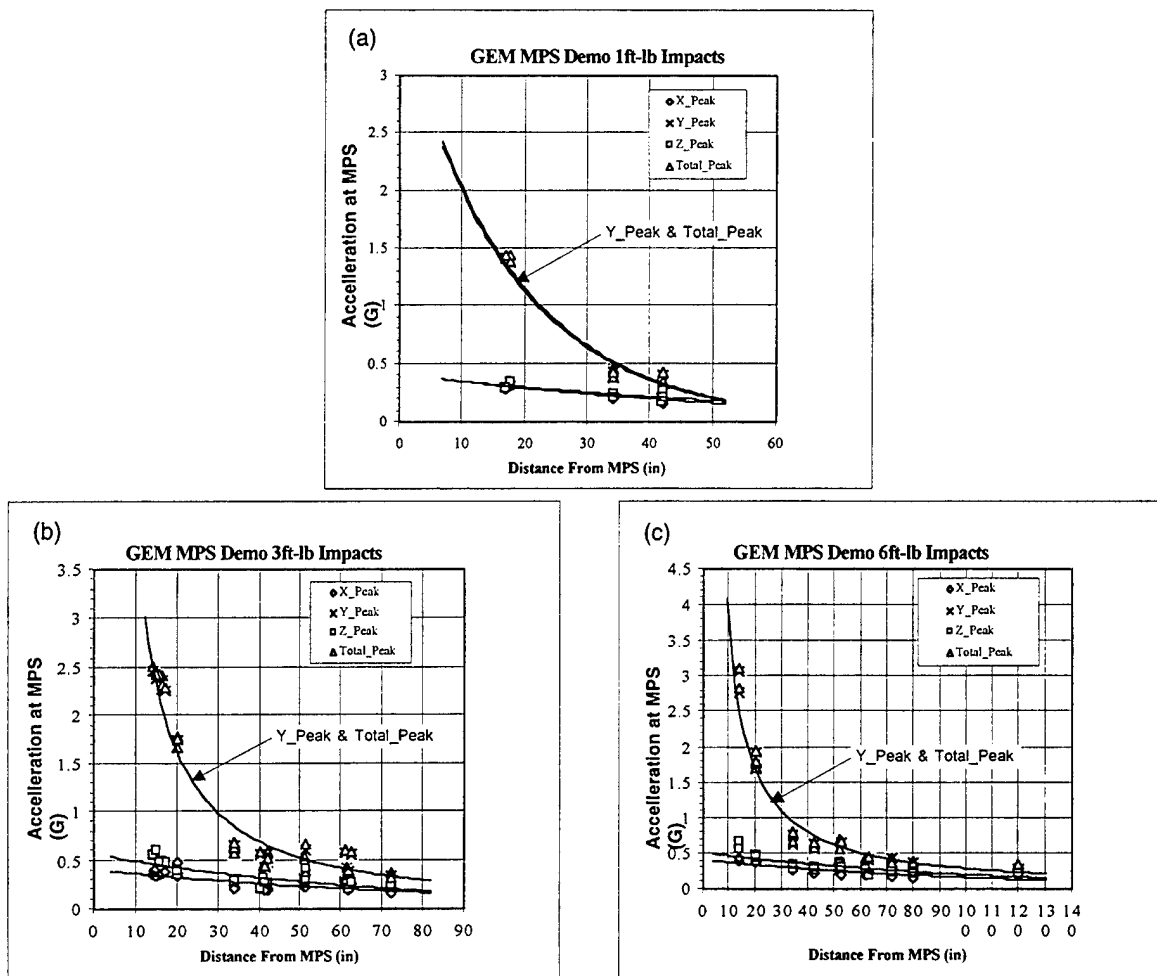
51

Figure 6-8. Peak Impact Acceleration vs. Position from MPS for (a) 1-ft-lb impact energy, (b) 3-ft-lb impact energy, (c) 6-ft-lb impact energy.

decrease the number of sensors and sensor spacing sufficiently to ensure that any damaging impact would be detected by at least two sensors, eliminating this problem.

Performance of the MPS accelerometer sensor may additionally be improved to increase sensitivity and to reduce the sensor noise floor. The present MPS design uses a ±50-G accelerometer. A ±5-G accelerometer would have been preferable for impact detection. Since the noise, in this case, is largely due to the read-out system, using the higher sensitivity accelerometer would proportionately lower the noise floor, potentially allowing for 10 milliGrms trigger threshold operation. Both of these sensor improvements would increase the detection distance range of the MPS impact monitor.

6.3.2   Environmental Sensor Data

Multiparameter environmental sensor data was derived from commercial MEMS and conventional sensors. MPS sensor performance data is shown in Table 6-1. In this demonstration, MPS data were sampled, averaged, and stored at the time of impact; however, it is expected that in actual use the

environmental portion of the data stream would be continuously data logged at a low rate to detect hazardous environments during storage and/or transportation. All MPS data were wirelessly transmitted to a roving remote laptop computer that stored the impact accelerations and environmental data.

Figure 6-9 shows the general trends in ambient temperature, atmospheric pressure, and relative humidity during the course of the test day. Increasing temperature during the day with a reduction in atmospheric pressure and a decrease in relative humidity were observed. In the data plots for temperature and pressure, there are anomalous data points early in the day and later in the afternoon. These data points are suspected to be due to changes in the test set-up stemming from differing power sources. Differing potentials from the laptop battery, auxiliary battery, or AC line adapter resulted in DC offsets in the sensor electronics of a few tens of millivolts. These differences resulted in the offset measurements and can be corrected in the future by the addition of improved line regulators.

From the environmental data shown, we demonstrated an ability to measure changes with a precision of better than 0.1°C in temperature, 0.1 kPa in pressure, and 0.5% in relative humidity. Based on manufacturer datasheet information, our accuracy was limited to ±0.8°C in temperature, ±3 kPa in pressure, and ±2 % in humidity. For this application, the MPS environmental monitors have more than sufficient resolution to detect and record most if not all storage, transportation, and launch base environments.

Table 6-1. MPS Sensor Performance

Sensor Type	Model	Data Range	Power Requirements
Temperature	Analog Devices AD592	−25°C to +105°C, ±0.8°C	4–30 VDC, 120 uA
Pressure	Motorola MPX5100A	15–115 kPa, ±3 kPa	4.75–5.25 VDC, 5–10 mA
Humidity	Ohmic HC-700	0–100% RH, ±2% RH	4–9 VDC, 0.2 to 2.0 mA
1 Axis Acceleration	Analog Devices ADXL150	±50 g	4.75–5.25 VDC, 1.8 mA
2 Axis Acceleration	Analog Devices ADXL250	±50 g	4.75–5.25 VDC, 3.6 mA

6.3.3　RF Datarates and Datapacket Loss Measurement

During our impact and handling test exercises, an additional experiment was conducted to determine the approximate datarate and datapacket error rate of the wireless network portion of the MPS system. Currently, all MPS data is collected in RAM on the data acquisition computer and then stored via wireless LAN to a remote hard disk at the user data terminal. In the GEM impact detection application, real-time data streaming is not required, although local high-bandwidth data collection is paramount. In other applications, such as remote control, process control, or battlefield sensor networks, real-time streaming data may be required. These wireless real-time-intensive applications will have their datarate impacted by the local rf transmission environment.

The present test was performed inside the warehouse/hangar where the GEM motor was located. The warehouse enclosure was approximately 100 ft wide by 200 ft long by 50 ft tall. The optimum direction of the MPS antennas was determined to be in the plane of the laptop keyboard, to the left of the operator. As part of the GEM MPS demonstration, the remote user data display computer was moved around the interior of the warehouse while datarate and datapacket error rates were determined. This experiment used a custom program that continuously broadcasts fixed data packets from the MPS
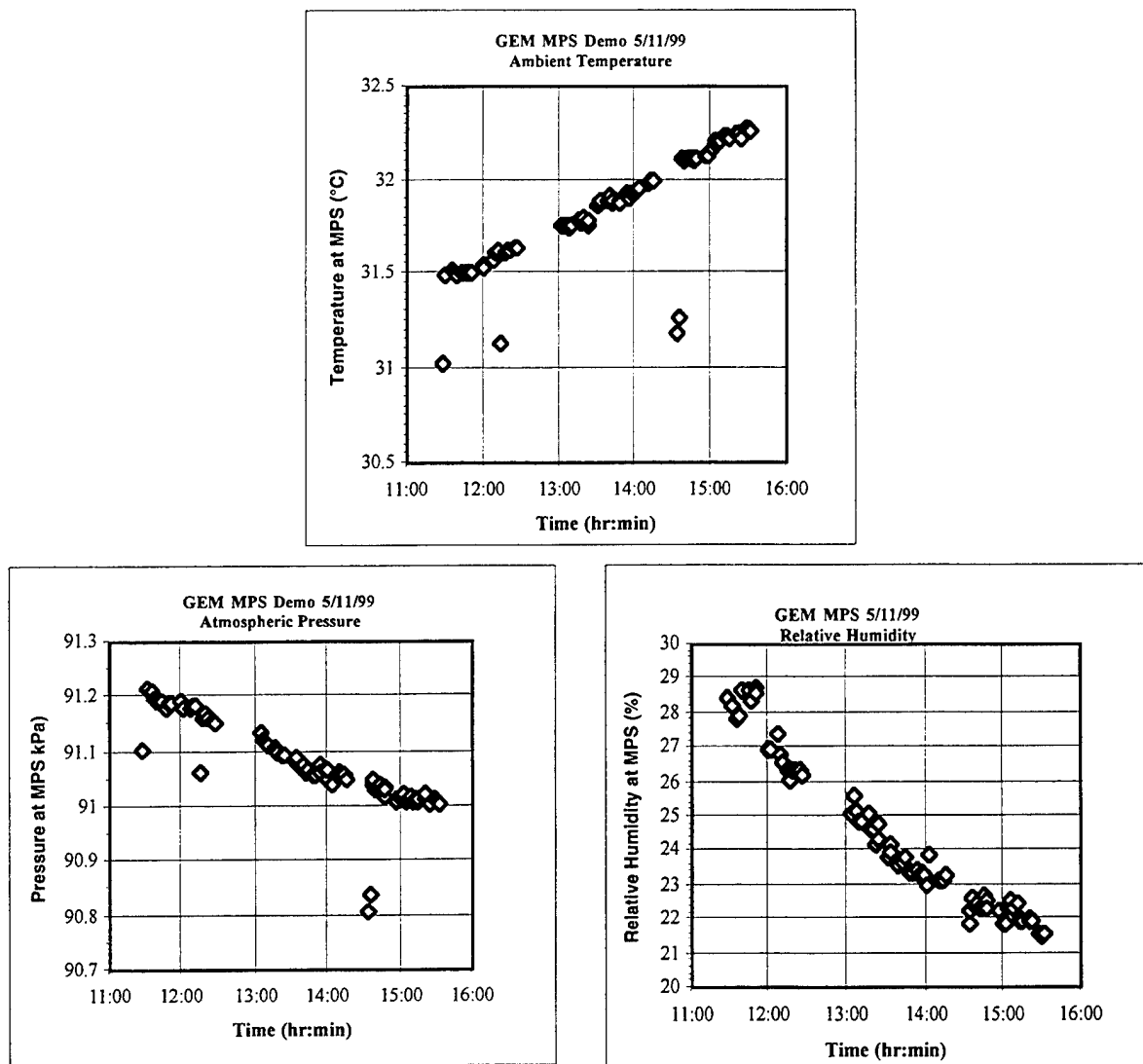
Figure 6-9.   MPS ambient temperature, pressure, and relative humidity during impact testing at
AFRL/EAFB rocket laboratory.

data collection system, while the remote user terminal logged wireless communication channel performance statistics.

Shown in Figures 6-10 and 6-11 are the results of this test. Figure 6-10 shows that the user terminal can expect to receive no less than 200 kb/s nor more than 400 kb/s. These values are to be compared with the maximum measured datarate of 1 Mb/s observed when outside and far away from all sources of interference. The wireless communication channel uses the same basic bit rate to communicate all the time; the effective datarate is lowered when, due to interference, datapackets are lost. Figure 6-11

shows the packet error rate plot of the warehouse environment. This figure shows that packet error rates range from 40% to 73% throughout the warehouse.

Although these rates will be different for any particular application, the results suggest that it is critical to survey the proposed application site to determine whether the desired wireless datarate performance can be achieved. Simple differences in configuration can have a dramatic effect on the resulting datarate, as seen in this case. One example of this can be seen in Figure 6-10. On the right side of the figure, the warehouse metal bay door was closed, while on the left side the bay door was open. The resulting multipath rf reflections off of the closed door resulted in an approximate 30% loss of datarate between the two ends of the warehouse.
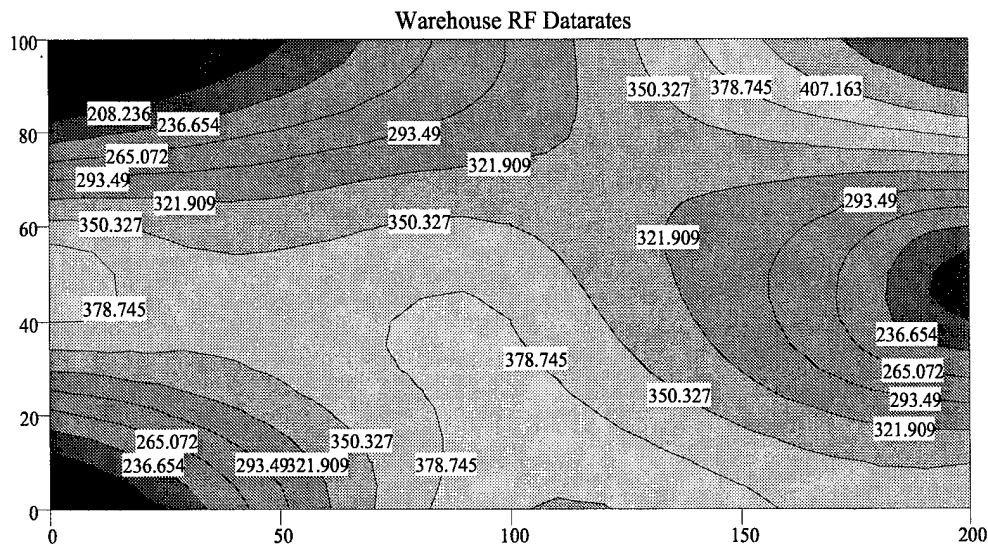

Figure 6-10.   MPS wireless datarates in positional relationship to the GEM casing. GEM casing is located in upper left corner. X-Y positions are in feet, datarates are in KBPS.
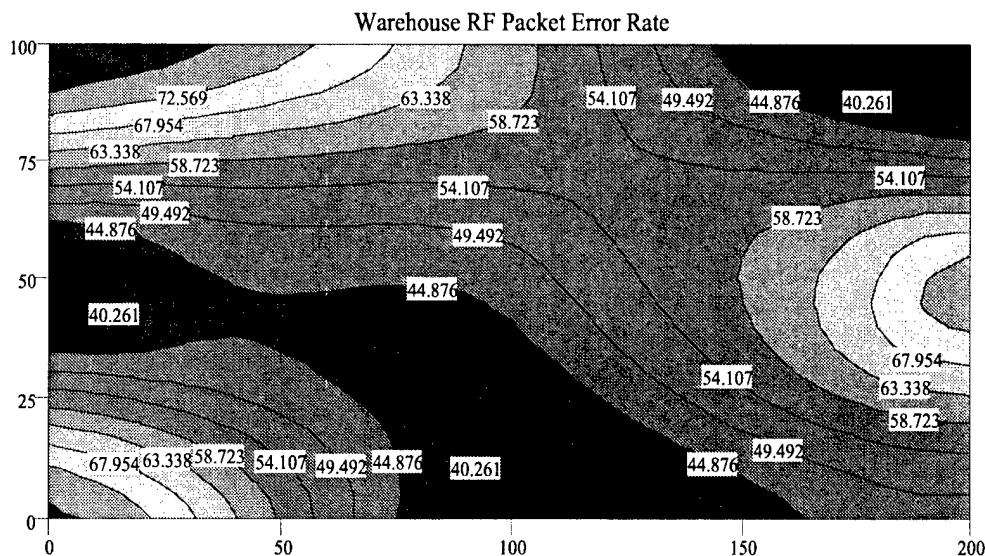
Figure 6-11.   MPS wireless datapacket error rates in positional relationship
to the GEM casing. GEM casing is located in upper left corner.
X-Y positions are in feet, error rates are in percent.

6.4   Conclusions

We have successfully demonstrated a prototype Delta GEM impact and environments health monitor
using the Aerospace Corporate Research Initiative MEMS Multiparameter Sensor (MPS) system.
Impacts slightly below the damage threshold were detected up to 10 ft away from the MPS system,
leading to the possibility of developing a simple, low-cost, distributed impact detector based on the
MPS with a distributed chain of accelerometers mounted along the body of the GEM casing. This
impact monitor would not determine absolute impact magnitude, or precise impact location, but
would alert the user that an impact above a predetermined threshold had occurred and within which
10-ft segment of the GEM the impact was located.

The MEMS sensors used in this demonstration provided a multi-parameter measurement of tempera-
ture, pressure, humidity, and three-axis acceleration. The environmental data collected showed nor-
mal daily trends in temperature, pressure, and humidity during the experiment run. This information
could be used, in practice, to determine that GEM casings were stored properly and not exposed to
excessive temperature, atmospheric humidity, or surface dew.

Finally, our wireless system was exercised in a typical warehouse environment and showed data rates
sufficient to support 8-bit sampling at 25 ksamples per second. This level of performance would be
sufficient for many wireless applications requiring real-time wireless data streaming from remote
MPS sensors.

6.5 Acknowledgements

6.6 References

1. "Delta II GEM, K522 Case Impact and Hydro/Structural Test Final Report," The Boeing Corporation, August 27, 1997, Contract F04701-93-C-0004, P00049, CDRL A004.

2. S. T. Amimoto, R. Crespo, E. W. Fournier, J. V. Osborn, H. Ozisik, B. H. Weiller, E. M. Yohnsee, "Development of Launch Vehicle Nanotechnology Instrumentation at The Aerospace Corporation," *Proceedings of the 44th International Instrumentation Symposium*, Aerospace Industries Division of ISA, Reno, NV, May 4-7, (1998)

3. S. T. Amimoto, R. Crespo, E. W. Fournier, J. V. Osborn, H. Ozisik, B. H. Weiller, E. M. Yohnsee, "Atlas Payload Transporter Vibration and Acceleration Characterization Using MEMS Sensors at Vandenberg AFB," Aerospace TOR-98(8260)-01 (1998).

4. Sherwin Amimoto, Brett Brown, Eric Fournier, Jon Osborn, Bruce Weiller, Brice Williams and Ernest Yohnsee "Sensor Node Development of a Low Power, High Data Rate Multi-Parameter Sensor (MPS) System," Space Technology and Applications International Form-1999, Albuquerque, NM

TECHNOLOGY OPERATIONS

The Aerospace Corporation functions as an "architect-engineer" for national security programs, specializing in advanced military space systems. The Corporation's Technology Operations supports the effective and timely development and operation of national security systems through scientific research and the application of advanced technology. Vital to the success of the Corporation is the technical staff's wide-ranging expertise and its ability to stay abreast of new technological developments and program support issues associated with rapidly evolving space systems. Contributing capabilities are provided by these individual organizations:

Electronics Technology Center: Microelectronics, VLSI reliability, failure analysis, solid-state device physics, compound semiconductors, radiation effects, infrared and CCD detector devices, data storage and display technologies; lasers and electro-optics, solid state laser design, micro-optics, optical communications, and fiber optic sensors; atomic frequency standards, applied laser spectroscopy, laser chemistry, atmospheric propagation and beam control, LIDAR/LADAR remote sensing; solar cell and array testing and evaluation, battery electrochemistry, battery testing and evaluation.

Mechanics and Materials Technology Center: Evaluation and characterizations of new materials and processing techniques: metals, alloys, ceramics, polymers, thin films, and composites; development of advanced deposition processes; nondestructive evaluation, component failure analysis and reliability; structural mechanics, fracture mechanics, and stress corrosion; analysis and evaluation of materials at cryogenic and elevated temperatures; launch vehicle fluid mechanics, heat transfer and flight dynamics; aerothermodynamics; chemical and electric propulsion; environmental chemistry; combustion processes; space environment effects on materials, hardening and vulnerability assessment; contamination, thermal and structural control; lubrication and surface phenomena.

Space and Environment Technology Center: Magnetospheric, auroral and cosmic ray physics, wave-particle interactions, magnetospheric plasma waves; atmospheric and ionospheric physics, density and composition of the upper atmosphere, remote sensing using atmospheric radiation; solar physics, infrared astronomy, infrared signature analysis; infrared surveillance, imaging, remote sensing, and hyperspectral imaging; effects of solar activity, magnetic storms and nuclear explosions on the Earth's atmosphere, ionosphere and magnetosphere; effects of electromagnetic and particulate radiations on space systems; space instrumentation, design fabrication and test; environmental chemistry, trace detection; atmospheric chemical reactions, atmospheric optics, light scattering, state-specific chemical reactions and radiative signatures of missile plumes.

Center for Microtechnology: Microelectromechanical systems (MEMS) for space applications; assessment of microtechnology space applications; laser micromachining; laser-surface physical and chemical interactions; micropropulsion; micro- and nanosatellite mission analysis; intelligent microinstruments for monitoring space and launch system environments.

Office of Spectral Applications: Multispectral and hyperspectral sensor development; data analysis and algorithm development; applications of multispectral and hyperspectral imagery to defense, civil space, commercial, and environmental missions.